OPEN ACCESS
IOP Publishing | International Atomic Energy Agency
Nuclear Fusion
Nucl. Fusion **66** (2026) 116007 (22pp)
https://doi.org/10.1088/1741-4326/ae6d12

# Progress and innovations in the TCV tokamak research programme

C. Theiler[1,*], J. Adamek[2], M. Agostini[3,4], C. Albert[5], S. Alberti[1], G. Alberti[6], S. Aleiferis[7], E. Alessi[8], G. Anastassiou[9], Y. Andrèbe[1], Y. Antonenas[9], G.M. Apruzzese[10], L. Aucone[11], F. Auriemma[3,4], J. Ayllon-Guerola[12], E. Aymerich[13], F. Bagnato[14,15], F. Bairaktaris[16], A. Balestri[1], J. Ball[1], S. Balugani[1], M. Baquero-Ruiz[1], O. Bardsley[7], A.F. Battey[1], T. Bauer[17], S. Bechtle[18], M. Bernert[19], W. Bin[8], P. Blanchard[1], J. Boedo[20], T. Bolzonella[3], L. Bonalumi[11], M. Bonisolli[1], T. Bosman[17,21], R. Bouffet-Klein[22], M.D. Boyer[23], L. Bramucci[3], F. Braunmüller[1], B.N. Breizman[24], D. Brida[19], B. Brown[1], S. Brunner[1], J. Buchli[18], J. Buermans[25,26], D. Busi[27], Y. Camenen[28], A. Cardinali[29], S. Carli[30], D. Carnevale[31], F. Carpanese[1], M. Carpita[1], A. Casolari[2], C. Castaldo[10], M. Cavedon[11], J. Cazabonne[32], J. Cerovsky[2], B. Chapman-Oplopoiou[7], O. Chellai[1], Y. Chervonyi[18], J. Chlum[2], P. Chmielewski[33], A. Chomiczewska[33], R. Cicioni[3], G. Ciraolo[32], I. Classen[21], A. Clod[34], S. Coda[1], C. Colandrea[1], C.E. Contré[1], R. Coosemans[1], L. Cordaro[3], M. Cornelissen[1,17,21], T. Craciunescu[35], D.J. Cruz Zabala[12], M. Czarski[33], I. Davies[18], C. Dawson[36], G. De Tommasi[37,38], B. De Vylder[18], J. Decker[1], G.L. Derks[17,21], E. Devlaminck[1], G. Di Giannatale[1], L.E. di Grazia[37], R. Ding[39], C. Donner[18], M. Dreval[40], C. Dritselis[41], S. Dubbioso[37,38], R. Ducker[1], M. Dunne[19], G. Durr-Legoupil-Nicoud[1], B.P. Duval[1], L. Édes[1], S. Ernst[1], M. Faitsch[19], C. Fan[36], A. Fasoli[1], N. Fedorczak[32], F. Felici[18], N. Ferron[3], O. Ficker[2], L. Figini[8], P. Figueiredo[17,21], A. Frank[1], L. Frassinetti[42], D. Frattolillo[37,38], D. Frigione[3], I. Furno[1], O. Février[1], D. Galassi[1], J. Galdon-Quiroga[12], S. Galeani[31], C. Galperti[1], M. Gambrioli[3], S. Garavaglia[8], S. Garcia Herreros[1], M. Garcia Munoz[12], P. Gaudio[31], M. Gelfusa[31], J. Genoud[1], S. Gerasimov[7], L. Gil[43], C. Giroud[7], P. Giroud-Garampon[1], M. Gobbin[3], T. Golfinopoulos[44], T.P. Goodman[1], S. Gorno[1], M. Grandin[3,45], G. Granucci[15], F. Graziano[27], M. Griener[19], N. Grzybicka[33], S. Guinchard[1], R. Hafner[18], A. Hakola[46], P. Halldestam[19], C. Ham[7], Ph. Hamel[18], D. Hamm[1], P. Heinrich[19], C. Heiß[1], S. Henderson[7], P. Hennequin[47], J.-P. Hogge[1], R. Hojlund[34], C. Honoré[47], M. Hoppe[42], J. Horacek[2], E. Huett[1], P. Innocente[3,4], P. Ivanov[1], V. Ivanov[48], T. Jackson[18], A. Jansen van Vuuren[1], A. Jardin[49], R. Jaspers[17], F. Jaulmes[2], T. Jensen[34], M. Jimenez Comez[12], E. Joffrin[32], D. Kabirov[12], A.N. Karpushov[1], S. Kasilov[5], Y. Kazakov[25], S. Kerboua-Benlarbi[1], A. Khan[1], D. King[7], A. Kirjasuo[46], E.M.M. Kivits[21], S. Kobussen[21], J.T.W. Koenders[17,21], P. Kohli[18], J. Kolsen de Wit[34], Y. Kominis[9], M. Kong[1], B. Kool[17,21], J. Kovacic[50], D. Kropackova[48], O. Krutkin[1], U. Kumar[1], R. Kwiatkowski[51], M. La Matina[3], B. Labit[1], A. Lafay[42], V. Laporta[52], N. Lazic[18], K. Lee[1], F. Lengyel[53,54], K. Lim[1], B. Linehan[44], A. Listopad[1], L. Lobko[48], N. Lonigro[7], T. Lunt[19], R. Mackenbach[1], E. Macusova[2], P. Maget[32], S. Malec[48], D. Mancini[1], P. Mantica[8], C. Marchetto[29], S. Marchioni[1], A. Mariani[8], M. Marin[1], A. Marinoni[55], M. Markl[5], Y. Martin[1], L. Martinelli[1], S. Masillo[1], R. Masocco[31], V. Masson[1], M. Mattei[37,38], S. Mattogno[31], D. Mazon[32], S. Mazzi[32], A. Mele[1], V. Menkovski[17], A. Merle[1], A. Michi[18], R. Mirowski[51], S. Misdanitis[41], R. Mishra[33], D. Moiraf[32], P.A. Molina-Cabrera[1], S. Molisani[3], F. Mombelli[6], R.I. Morgan[1],

[*] Author to whom any correspondence should be addressed.



 

**A. Moro[8], A. Murari[3,4], K. Murray[56], P. Muscente[3,44], I. Muzio[1], D. Mykytchuk[1], Y. Nakeva[57], F. Napoli[10], A.H. Nielsen[34], S.K. Nielsen[34], T. Norman[18], S. Nowak[8], H. Nyström[42], R. Ochoukov[19], A. Orduna-Martinez[19], L. Orlandi[3], C. Orrico[17,21], F.P. Orsitto[37], R. Osawa[7], N. Osborne[7,56], P. Oyola[12,58], C. Paduaru[18], A. Pajares[59], D.I. Palade[35], O. Pan[19], O. Panico[1], P. Papagiannis[9], M. Passoni[6], F. Pastore[1], A. Patel[19], A. Pau[1], C. Paz-Soldan[60], A.C. Pedersen[34], M. Pedrini[1], G. Pelka[33], A. Perek[1], Y. Peres Asnis[1], R. Perillo[20], F. Pesamosca[14,19], K. Petersen[34], L. Pigatto[3], C. Piron[3,10], L. Piron[3], A. Pironti[37,38], V. Plyusnin[43], M. Podesta[1], Y. Poels[1], G.I. Pokol[53,54], J. Poley[1], L. Pomârjanschi[35], M. Poradzinski[33], L. Porte[1], C. Possieri[31], F. Puentes del Pozo[12], M.J. Pueschel[17,21], V. Quadri[32], M. Rabinski[51], R. Ragona[34], G.A. Ratta[61], C. Rea[44], H. Reimerdes[1], M. Reisner[19], C. Reux[32], D. Ricci[8], P. Ricci[1], M. Riedmiller[18], S. Rienäcker[47], N. Rispoli[8], J.F. Rivero-Rodriguez[7,12], R. Rizkallah[20], A. Rodriguez Gonzalez[12], F. Romano[1], R. Rossi[31], M. Rud[1,34], D. Sales de Oliveira[1,32], M. Salewski[34], A. Salmi[46], O. Sauter[1], Bo S Schmidt[34], N. Schoonheere[32], K. Schutjes[17,21], L. Scotti[11], L. Senni[10,62], M.G. Senstius[63], S. Setzu[13], S.E. Sharapov[7], U.A. Sheikh[1], G. Sias[13], M. Silva Füglister[1], D. Silvagni[19], A. Simonetto[8], L. Simons[1], L. Singh[32], K. Singh[1], P. Sintre[1], S. Sipilä[64], O. So[36], C. Sommariva[1], C. Sozzi[8], S. Spagnolo[3,4], A. Stagni[3,45], C. Stollberg[1], F. Subba[65], G. Sun[1], H. Sun[1], J. Svantner[1], T. Tala[46], P. Tamain[32], K. Tanaka[66], W. Tang[19], A. Tema Biwole[1], A. Tenaglia[31], D. Terranova[3,4], D. Testa[1], K.E. Thome[59], A. Thrysoe[34], M. Tomes[2], E. Tonello[1], M.A. Topalova[67], B. Tracey[18], E. Tsitrone[32], C.K. Tsui[68], J. Tumbokon[1], M. Tunkl[26,48], M. Ugoletti[4], A. Valentini[34], M. Vallar[1], M. Van Berkel[21], L. van Leeuwen[17,21], S. Van Mulders[1,14], G. Van Parys[1], M. Van Rossem[1], C. Venturini[1], K. Verhaegh[17], L. Vermare[47], N. Vianello[3,4], E. Viezzer[12], L. Villard[1], B. Vincent[1], C. Vincent[7], P. Vincenzi[3,4], J. Vinklárek[48], I. Voitsekhovitch[7], L. Votta[42], N.M.T. Vu[14], A. Wang[36,44], C. Wang[1], Y. Wang[1], N. Wendler[33], E. Westerhof[21], S. Wiesen[21], T. Wijkamp[21], M. Winkel[17], C. Wüthrich[1], I. Wyss[31], L. Xiang[7], G. Xu[39], H. Yang[69], J. Zebrowski[51], P.A. Zestanakis[9], H. Zhang[1], C.F.B. Zimmermann[60], M. Zuin[3,4] and M. Zurita[1]**

[1] École Polytechnique Fédérale de Lausanne (EPFL), Swiss Plasma Center (SPC), Lausanne, Switzerland
[2] Institute of Plasma Physics of the CAS, Prague, Czech Republic
[3] Consorzio RFX (CNR, ENEA, INFN, University of Padova, Acciaierie Venete SpA), Corso Stati Uniti 4, Padova, Italy
[4] Istituto per la Scienza e Tecnologia dei Plasmi ISTP-CNR, Padova, Italy
[5] Fusion@ÖAW, Institute for Theoretical Physics—Computational Physics, Graz University of Technology, Graz, Austria
[6] Department of Energy, Politecnico di Milano, Milan, Italy
[7] United Kingdom Atomic Energy Authority, Culham Campus, Abingdon, Oxfordshire, United Kingdom of Great Britain and Northern Ireland
[8] Istituto per la Scienza e Tecnologia dei Plasmi ISTP-CNR, Milano, Italy
[9] School of Applied Mathematical and Physical Sciences, National Technical University of Athens, Athens, Greece
[10] Unità Tecnica Fusione, ENEA, Frascati, Italy
[11] Università di Milano-Bicocca, Milano, Italy
[12] Universidad de Sevilla, Sevilla, Spain
[13] Dept. of Electrical and Electronic Engineering, University of Cagliari, Cagliari, Italy
[14] ITER Organization, Saint-Paul-lez-Durance, France
[15] DTT S.C.a.r.l., Frascati, Italy
[16] School of Electrical and Computer Engineering, National Technical University of Athens, Athens, Greece
[17] Eindhoven University of Technology, Eindhoven, Netherlands
[18] Google DeepMind, London, United Kingdom of Great Britain and Northern Ireland
[19] Max Planck Institute for Plasma Physics, Garching, Germany
[20] Center for Energy Research (CER), University of California-San Diego (UCSD), La Jolla, CA, United States of America
[21] DIFFER-Dutch Institute for Fundamental Energy Research, Eindhoven, Netherlands
[22] ENS Paris-Saclay, Gif-sur-Yvette, France
[23] Commonwealth Fusion Systems (CFS), Devens, MA, United States of America
[24] Institute for Fusion Studies, The University of Texas, Austin, TX, United States of America
[25] Laboratory for Plasma Physics, LPP-ERM/KMS, Brussels, Belgium

[26] Department of Applied Physics, Ghent University, Ghent, Belgium
[27] Department of Mechanical Engineering, Politecnico di Milano, Milan, Italy
[28] CNRS, Aix-Marseille Univ., PIIM UMR7345, Marseille, France
[29] Dipartimento Energia, CNR-ISC and Politecnico di Torino, Torino, Italy
[30] Department of Mechanical Engineering, KU Leuven, Leuven, Belgium
[31] University of Rome Tor Vergata, Rome, Italy
[32] CEA, IRFM, F-13108 Saint Paul-Lez-Durance, France
[33] Institute of Plasma Physics and Laser Microfusion (IPPLM), Warsaw, Poland
[34] Department of Physics, Technical University of Denmark, Kgs, Lyngby, Denmark
[35] National Institute for Laser, Plasma and Radiation Physics, Bucharest-Magurele, Romania
[36] Laboratory for Information and Decision Systems (LIDS), Massachusetts Institute of Technology, Cambridge, MA, United States of America
[37] Consorzio CREATE, Napoli, Italy
[38] Università degli Studi di Napoli 'Federico II', Napoli, Italy
[39] Institute of Plasma Physics, Hefei Institutes of Physical Science, Chinese Academy of Sciences, Hefei, China
[40] Institute of Plasma Physics of the NSC KIPT, Kharkov, Ukraine
[41] Department of Mechanical Engineering, University of Thessaly, Volos, Greece
[42] Department of Electromagnetics and Plasma Physics, KTH Royal Institute of Technology, Stockholm, Sweden
[43] Instituto de Plasmas e Fusao Nuclear, Instituto Superior Técnico, Universidade de Lisboa, Lisboa, Portugal
[44] Plasma Science and Fusion Center (PSFC), Massachusetts Institute of Technology, Cambridge, MA, United States of America
[45] CRF—University of Padova, Padova, Italy
[46] VTT Technical Research Centre of Finland Ltd., Espoo, Finland
[47] Laboratoire de Physique des Plasmas (LPP), CNRS, Sorbonne Université, École polytechnique, Institut Polytechnique de Paris, Palaiseau, France
[48] Faculty of Nuclear Sciences and Physical Engineering, Czech Technical University in Prague, Prague, Czech Republic
[49] Institute of Nuclear Physics Polish Academy of Sciences (IFJ PAN), Krakow, Poland
[50] Faculty of Mechanical Engineering, University of Ljubljana, Ljubljana, Slovenia
[51] National Centre for Nuclear Research (NCBJ), Otwock, Poland
[52] Istituto per la Scienza e Tecnologia dei Plasmi, Bari, Italy
[53] HUN-REN Centre for Energy Research, Budapest, Hungary
[54] Department of Nuclear Techniques, Budapest University of Technology and Economics, Budapest, Hungary
[55] Fusion Engineering Institute, University of California at San Diego (UCSD), La Jolla, CA, United States of America
[56] University of Liverpool, Liverpool, United Kingdom of Great Britain and Northern Ireland
[57] Department of Economics, Engineering, Society and Business Organization (DEIm), University of Tuscia, Viterbo, Italy
[58] Princeton Plasma Physics Laboratory (PPPL), Princeton, NJ, United States of America
[59] General Atomics, San Diego, CA, United States of America
[60] Columbia University, New York, NY, United States of America
[61] Laboratorio Nacional de Fusión, CIEMAT, Madrid, Spain
[62] Institute for Applied Mathematics IAC—CNR, Roma, Italy
[63] Rudolf Peierls Centre for Theoretical Physics, University of Oxford, Oxford, United Kingdom of Great Britain and Northern Ireland
[64] Aalto University, Espoo, Finland
[65] NEMO Group, Politecnico di Torino, Torino, Italy
[66] National Institute for Fusion Science, Toki, Gifu, Japan
[67] University of Manchester, Manchester, United Kingdom of Great Britain and Northern Ireland
[68] Sandia National Laboratories, Livermore, CA, United States of America
[69] M2P2, Aix-Marseille Univ, CNRS, Centrale Méditerranée, Marseille, France

E-mail: christian.theiler@epfl.ch

Received 16 December 2025, revised 17 March 2026
Accepted for publication 13 May 2026
Published 5 June 2026


**Abstract**

Research on the Tokamak à Configuration Variable addresses a wide range of key questions relevant to ITER and future fusion power plants. Over the past two years, highly productive experimental campaigns have led to major advances across several areas: the ITER

baseline scenario; pedestal properties in low-collisionality, peeling-limited conditions; and the development of high-$\beta_N$, non-inductive regimes. Alternative high-confinement scenarios have likewise received significant attention, with remarkable progress in quasi-continuous exhaust operation, X-point radiator plasmas, and negative triangularity configurations. Substantial achievements were also made in the mitigation or benign termination of runaway electron beams, in elucidating fast-ion loss mechanisms, and in improving exhaust behaviour in both conventional and alternative divertor geometries. These experimental results have been strongly supported by advances in modelling and their direct application to the experiment, ranging from gyrokinetic simulations of core and pedestal turbulence to fluid-based studies of scrape-off layer and divertor physics in diverse geometries. Plasma control has taken on an increasingly important role, with model-based and data-driven approaches now closely intertwined with physics studies. This article provides a overview of these recent activities, together with a brief outlook on forthcoming upgrades and next steps.

Keywords: magnetic confinement fusion, tokamak, plasma, TCV, review, EPFL

(Some figures may appear in colour only in the online journal)

## 1. Introduction

The Tokamak à Configuration Variable (TCV, major radius $R \approx 0.88$ m, aspect ratio $A \approx 3.5$, toroidal field $B \leqslant 1.5$ T, full carbon wall) is a highly flexible research facility operated at the Swiss Plasma Center (SPC) of the Swiss Federal Institute of Technology Lausanne (EPFL) [1, 2]. It features unique magnetic shaping capabilities, excellent diagnostics, a modern control system, and versatile heating systems—currently consisting of 2.6 MW Neutral Beam Injection (NBI) and a total of 3.5 MW of second (X2) and third (X3) harmonic Electron Cyclotron Resonance Heating (ECRH) power. Two additional, 1 MW, dual-frequency gyrotrons are foreseen for 2026–2027. Operated partly as a European facility within the EUROfusion Tokamak Exploitation Work Package (WPTE) [3], research on TCV tackles key challenges for ITER and fusion power plants while contributing strongly to the education of young researchers.

Following a complete overhaul of neutron and gamma-ray shielding in early 2023, TCV now operates without radiation-imposed limits despite recent increases in NBI power capabilities [4]. The fourth major refurbishment of TCV's flywheel generator made it ready for the next ten years of operation [5] and improvements in the preparation and data-quality monitoring of the standard TCV diagnostics improved experimental efficiency [6]. The 2023-2025 campaigns were highly productive, featuring four different divertor closures and attaining a record of 3'517 successful plasma discharges in 2024, while simultaneously preparing for various upgrades.

This article provides an overview of the results achieved during this period. Section 2 discusses progress in ITER Base-Line (IBL), steady-state and alternative ELM-free scenarios. This is followed by electron runaway studies in section 3 and Alfvén eigenmode (AE) and fast ion (FI) studies in section 4. Additional topics related to core physics (section 5), edge/-pedestal physics (section 6) and SOL and divertor physics (section 7) follow. The article concludes with a summary of the progress in plasma control (section 8) and with a brief outlook (section 9).

## 2. Plasma scenarios—H-mode and alternative ELM-free regimes

### 2.1. IBL and steady-state scenarios

TCV has devoted significant efforts to studying and preparing for the operation of the 'standard' inductive ELMy H-mode scenario foreseen for ITER, the IBL. NBI and ECRH heated IBL scenarios were developed and analysed [7], using the strategy to enter H-mode at large $q_{95}$ and reduced shaping. Three different ITER shapes were reproduced, the JET IBL, the AUG IBL, and the ITER IBL. The experiments displayed increasing ELM perturbations and enhanced difficulty to reach stationary conditions for increasing top triangularity. Good performance ($H_{98} \sim 1.2, \beta_N \sim 1.6$) was demonstrated for several energy confinement times, usually followed by the onset of neoclassical tearing modes (NTMs). Avoidance of this NTM onset with X3 heating succeeded at medium $\beta_N$ and high $q_{95}$, but was constrained at ITER $q_{95}$ due to density peaking and weak X3 absorption. Integrated modelling using ASTRA-GLF23 quasi-linear drift model-based transport identified ITGs as the dominant core instability in these plasmas and reproduced the turbulent-driven density peaking. More recent scenarios with up to 90% X3 absorption featured large, regular ELMs and avoided NTMs but at lower $q_{95}$ than the IBL.

A parameter that cannot be matched in IBL studies on today's devices is the pedestal collisionality. As part of a EUROfusion multi-device effort that also includes JET and MAST-U, significant work has been dedicated to extending pedestal studies on TCV towards ITER-relevant, low-$\nu^\star$, peeling-limited conditions [8]. This was pursued by operating at low density and high power with both NBI and ECRH, reaching Type-I ELMy regimes with pedestals limited by peeling instabilities. $D_2$ fuelling scans showed that, unlike in ballooning-limited pedestals, the pedestal pressure increases with $n_{e,ped}$, figure 1(*a*), a behaviour ascribed to the stabilising effect of density on peeling modes. Consistently with JET and MAST-U, the TCV results furthermore showed that the

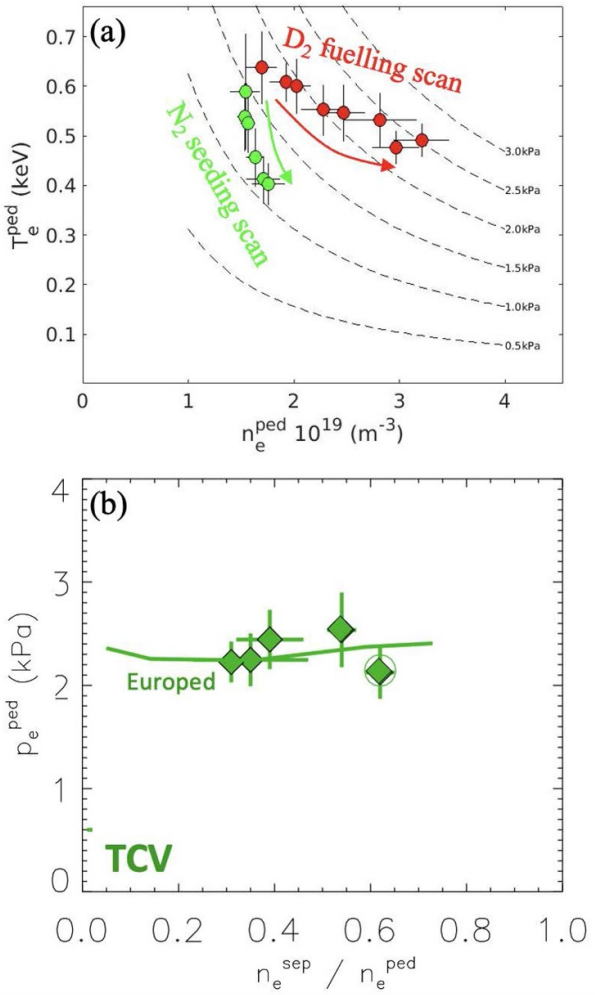


**Figure 1.** Key properties of low-$\nu^\star$ pedestals limited by peeling instabilities in TCV. (*a*) Effect of fuelling and $N_2$ seeding scans on pedestal properties, showing increasing pedestal pressure with fuelling and decreasing pedestal pressure with seeding. The dashed lines indicate isobars of constant pedestal pressure, and the arrows indicate the direction of increasing gas injection rate. While the former behaviour is ascribed to the stabilising effect of density on peeling modes, the latter is not yet understood. (*b*) Non-degradation of pedestal pressure with the ratio of separatrix to pedestal density, observed experimentally and reproduced with Europed. Reproduced from [8]. 

pedestal pressure does not degrade with increasing $n_{e,sep}/n_{e,ped}$ in these low-$\nu^\star$ conditions, figure 1(*b*). These results are consistent with Europed, and preliminary extrapolations suggest that this favourable behaviour extends to ITER conditions. Extension of these studies from deuterium to hydrogen plasmas showed qualitatively similar results. In contrast, the pedestal pressure was found to degrade with $N_2$ seeding, figure 1(*a*), for reasons that are not yet understood [8]. Interestingly, contrary to high-$\nu^\star$ plasmas, $N_2$ seeding at low-$\nu^\star$ showed also a pronounced effect on the Scrape-Off Layer (SOL) profiles, resulting in a *decrease* of the near-SOL density decay length and a reduction in the far-SOL density shoulder [9].

A key aspect in view of ITER operation is an improved understanding of the power threshold for accessing H-mode, $P_{\rm LH}$, and its various dependencies. To this end, systematic $P_{\rm LH}$ studies, which were previously carried out primarily in Ohmic plasmas on TCV via $I_p$ ramps, have been extended to predominantly NBI-heated plasmas [10]. With the plasma shape held fixed, a broad parameter space was explored by scanning the core density, plasma current, and the main ion species (H, D, He) as well as their mixtures. For deuterium plasmas at $q_{95} \approx 3.3$, the observed scaling aligns well with the ITPA scaling law. The most notable result was that, across all densities, $P_{\rm LH}$ increased as $I_p$ was reduced, consistent with the interpretation that improved L-mode confinement facilitates the L–H transition.

Following TCV's extensive history of steady-state, fully non-inductive operation using X2 Electron Cyclotron Current Drive (ECCD), and in preparation for long-pulse scenarios on JT-60SA and ITER, significant recent progress has been made in experimentally developing advanced scenarios with more balanced $T_e$ and $T_i$ [11]. Guided by ASTRA modeling, various heating and current drive configurations were established, combining the three existing X2 gyrotrons—each with independent launchers—and the two NBIs. A narrow operational range in density, constrained by the ECRH-X2 cutoff and NBI coupling efficiency, required good density control and specific timing of the heating sources. Non-inductive internal transport barrier (ITB) scenarios transiently achieved record core $T_e$ values of 12 keV and $\beta_N \approx 1.85$, but were restricted to the ECRH-only phase and to $T_e \gg T_i$. The addition of NBI heating led to a progressive degradation in performance. A more promising route proved to be approaches with more balanced NBI-1, NBI-2, and ECRH, evolving into a fully non-inductive semi-stationary scenario with $\beta_N \approx 2$, figure 2. Although gradients in density and temperature increased locally at mid-radius and near the edge, a strong ITB or edge transport barriers (ETBs) were not observed. As a result, the bootstrap current fraction remained modest ($\sim 30\%$). A promising strategy to address this limitation involves the forthcoming fourth X2 gyrotron, which will enable more central heating. This will complement the existing gyrotrons used in off-axis co-ECCD, enhancing sustainment of the scenario. With these advancements, there is now a realistic prospect of achieving a fully stationary, high-$\beta_N$, non-inductive, NBI-heated scenario. A fully central-solenoid-free current ramp-up, from 30 ms after breakdown, was also achieved with the sustainment of an electron ITB [11].

### 2.2. *Alternative high-confinement scenarios*

Alternative, high-confinement scenarios without large Type-I ELMs continued to be a strong focus on TCV [12]. One promising candidate is the quasi-continuous exhaust (QCE) regime, a well-established operational mode achieved at high shaping and high fuelling. Its access is attributed to unstable ballooning modes localised near the separatrix, which prevent the pedestal from reaching the global peeling-ballooning limit and thus suppress the onset of Type-I ELMs. Consistent with this interpretation, a multi-diagnostic turbulence study

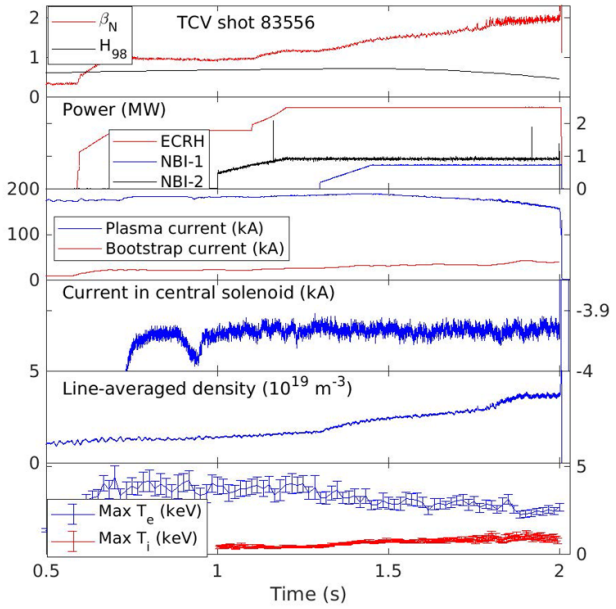


**Figure 2.** Time traces of a fully non-inductive, semi-stationary scenario combining ECRH and NBI heating, reaching $\beta_N \approx 2$ and higher $T_i/T_e$ than in previous, ECRH-only scenarios. Reproduced from [11]. © 2026 The Author(s). Published by IOP Publishing Ltd on behalf of the IAEA. CC BY 4.0.

identified a weakly coherent mode just inside the separatrix, at $f \approx 50$ kHz and $k_\theta \approx 100$ m$^{-1}$[13]. Progress in understanding the QCE regime, supported by a step-ladder approach involving TCV and AUG, has led to the successful development of the QCE in JET [12, 14]. Experiments on the three devices revealed a trend of decreasing collisionality for QCE operation with increasing machine size, which, together with predictive modelling, points to QCE as a potential default operational regime for ITER and DEMO.

The SOL properties in the QCE regime have been investigated in high-density H-mode plasmas by increasing the upper triangularity from 0.0 to 0.6, resulting in a transition from Type-I ELMy H-mode to QCE [15]. Both the SOL fall-off lengths of power ($\lambda_q$) and density ($\lambda_n$) increased by a factor of 2.5 across this scan, correlating with the turbulence control parameter $\alpha_t$ and suggesting a transition to resistive ballooning-dominated SOL turbulence under high-density H-mode conditions. However, this advantageous behaviour of the QCE in view of divertor power exhaust was also associated with the formation of a density shoulder. This shoulder formation correlated with an increased filament frequency at the first wall and raises questions in terms of main-chamber plasma-wall interactions in the QCE.

The X-Point Radiator (XPR) is another attractive alternative H-mode regime. It offers high radiated power fraction and often achieves full detachment and full ELM suppression, though at the cost of a potential increase in core impurity concentrations and confinement degradation [16]. The existence of an XPR in LSN, seeded H-mode on TCV has been demonstrated both experimentally and through SOLPS-ITER simulations [17]. Its operating window, however, was found to be narrow, as predicted by analytical models for C-wall machines. This window was dramatically broadened by modifying the magnetic geometry [18]. Positioning a secondary X-point near the separatrix, at some distance from the primary X-point in a snowflake-minus shape, enabled the transition to a stable, fully ELM-suppressed XPR without impurity seeding. Confinement and pedestal parameters remained comparable to the preceding Type-I ELMy phase, while $Z_{\text{eff}}$ increased by approximately 50%. This snowflake-minus geometry features a long connection length from the outboard midplane to just above the primary X-point, an extended interface with the high neutral density reservoir in the private flux region, and large poloidal flux expansion in the X-point region toward the core—all features that are theoretically expected to facilitate XPR access. In contrast, configurations closer to an ideal snowflake, sharing only some of these features, did not enable access to the regime. Interestingly, these experiments also showed that an XPR with ELM suppression is not synonymous with divertor detachment. Overall, this work provides an excellent testbed for further XPR model validation.

Negative triangularity (NT) core plasmas, pioneered on TCV, offer a promising route to achieving high-confinement operation while remaining in L-mode, thereby avoiding ELMs and the constraint of operating above the L–H power threshold. Significant recent progress has been achieved in the development of NT scenarios with high input power and high core-performance using NBI [19], see figure 3. These scenarios reach stationary conditions with $\beta_N \sim 1.7$ and $H_{98} \sim 1.3$, close to those in positive triangularity (PT) H-mode operation on TCV. They are compatible with the TCV baffles and feature higher central ion and electron temperatures than equivalent PT L- and H-mode scenarios. Substantial progress was achieved in divertor detachment and core-edge integration of these and other NT scenarios, and in the theoretical understanding and extrapolation capabilities of NT physics, as detailed in the following.

Ohmic L-mode detachment of the outer divertor via core density ramps was investigated across a wide range of upper, lower, and average triangularity, universally finding detachment more difficult to achieve in NT [20]. While partly explained by differences in divertor geometry, as supported by SOLPS-ITER simulations applying the same transport coefficients in NT and PT [21], significant differences persisted in geometries with fixed divertor geometry, where only the upper triangularity was varied. Increasing the neutral pressure in NT using TCV's divertor baffles, approaching the levels in unbaffled PT plasmas, reduced the outer target temperature. However, detachment remained more difficult to achieve than in PT [22]. These results could at least partly be explained by a narrower $\lambda_q$ in NT than in PT L-mode, an effect understood theoretically [23] and confirmed experimentally [24]. In particular, the experimental work in [24] clearly identified a dependence of $\lambda_q$ on the upper (non-X-point) triangularity, while no dependence on the lower triangularity was observed. Simulations with SOLPS-ITER [25] and SOLEDGE2D-EIRENE [26] suggested that a reduction in

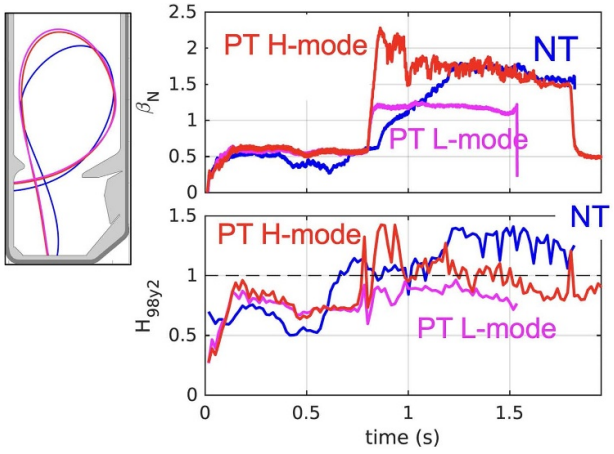


**Figure 3.** Time histories of normalised beta and *H*-factor for baffled, NBI-heated discharges with positive and negative top triangularity; the corresponding plasma shapes are highlighted on the left. The NT discharge (0.75 MW NBI) shows substantially improved performance compared to the PT L-mode (0.75 MW NBI) and approaches that of the PT H-mode (1.3 MW NBI), even during the latter's best-performing phase (0.9–1.0 s). Reproduced from [19]. 

particle rather than heat diffusivity in NT is needed to match the experimental findings. Despite these challenges, in the baffled, high-performance NT NBI scenarios, outer divertor detachment with an XPR was achieved through nitrogen seeding [19]. Combining this core scenario with a snowflake divertor further allowed for a substantial cooling of the inner strikepoint as well [27]. As in PT H-mode, core performance degraded with seeding, but could be recovered through real-time adjustments of NBI power, overall highlighting NT's potential for core-edge integration.

Theoretical studies and gyrokinetic simulations of core turbulence and transport in NT—motivated by and partly validated on TCV—have improved our understanding and extrapolation capabilities. In Ion Temperature Gradient (ITG) dominated plasmas simulated with GENE, NT was predicted to be more stable than PT for any value of aspect ratio $A$ and for any plasma elongation $\kappa > 1$ [28, 29]. For Trapped Electron Mode (TEM) dominated turbulence, instead, the benefits of NT were found to be limited to large and conventional $A$. Global ORB5 simulations with kinetic trapped electrons predict that the transport reduction of NT relative to PT is independent of system size, suggesting that the favourable transport properties of NT could extrapolate well to reactor conditions [30]. At reactor-relevant, high $\beta_N$, electromagnetic instabilities like Micro-Tearing Modes (MTMs) tend to dominate and these modes were found to be more unstable in NT than in PT. However, due to the low magnetic shear in DEMO-scale devices, simulations predicted ITG-dominated turbulence, where NT remained highly favourable [29]. TCV experiments and numerical investigations of PT and NT plasmas in the shapes foreseen for the Divertor Tokamak Test (DTT) facility showed promising results, despite DTT's limited NT shaping capabilities, supporting future NT studies at larger size and higher field than possible today [31, 32].

## 3. Disruptions and runaway-electrons

Runaway Electron (RE) beams constitute a major threat for a reactor, from discharge startup to termination. Recent TCV experiments [34] demonstrated that central ECRH heating induces enhanced transport, which combines with decreased RE seed generation due to lower loop voltage to reduce existing RE seed populations by up to three orders of magnitude. In a reactor context, such seed expulsion could expel startup REs and avoid post-disruption RE formation or avert a transition to the dangerous slideaway regime. Additional work is needed to determine the effect of ECRH on an existing RE seed in larger tokamaks and to assess how the required ECRH power scales with machine size. Complementary to seed expulsion, RE dynamics could also be influenced by momentum-space effects. The resonant interaction between the RE gyromotion and the toroidal magnetic field ripple was shown to explain the anomalously high RE pitch angles in TCV, providing direct experimental evidence of RE momentum-space engineering [35]. This effect resulted in enhanced synchrotron radiation power loss, limiting RE energy.

Once a post-disruption RE beam has formed, the focus shifts to its termination. Low-$Z$ Benign Termination (BT), relying on large MHD instabilities to expel REs over a broad wetted area while converting magnetic energy into radiation, has emerged as a promising strategy [36]. BT requires the background companion plasma to have low electron density, achieved in a specific neutral pressure range, which enables the fast growing MHD instability required, figure 4. The lower limit of this range was studied, for the first time, with SOLPS-ITER, reproducing experimental trends and highlighting the importance of power dissipation via neutral energy conduction to the walls [37]. The upper neutral pressure limit for BT was explored with a particle balance model and through comparisons with experiments [33], indicating that RE impact ionisation plays a significant role in increasing the companion plasma density. A multi-device study, including AUG, COMPASS, DIII-D, JET, and TCV, predicts a neutral pressure range of 0.2 Pa–1.5 Pa for BT in ITER, which is substantially lower than the pressures expected in the current ITER staggered disruption mitigation injection scheme, requiring further studies [36].

RE studies on TCV have benefited, and continue to improve, from diagnostic improvements. A new gamma-ray detector, LaBrDoREs (Lanthanum Bromide Detector of Runaway Electrons), was developed [38], which allows monitoring the RE population by measuring the Bremsstrahlung emission in the 1–30 MeV range, generated when REs interact with plasma-facing components or particles in their path. TCV's unique Fast Ion Loss Detector (FILD) allowed, for the first time in magnetically confined plasmas, to obtain direct velocity-space resolved measurements of RE losses [39].

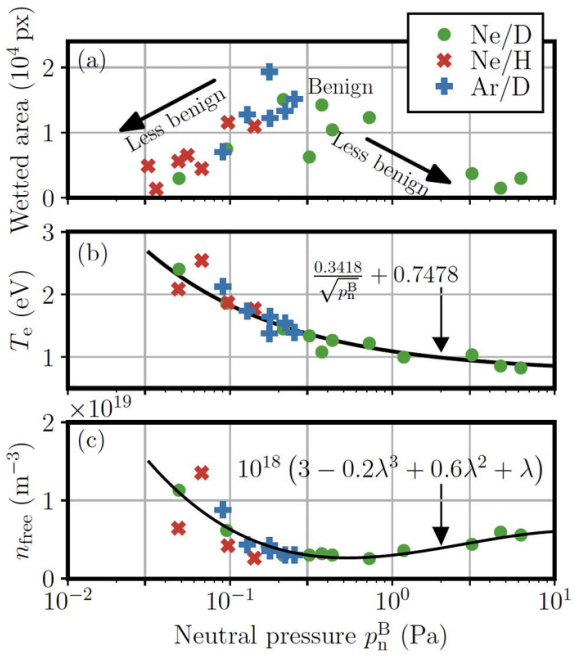


**Figure 4.** Neutral pressure dependence of (*a*) the wetted area and (*b*), (*c*) the temperature and density of the background companion plasma during post-disruption RE beam termination experiments. The wetted area is defined as the number of pixels above a temperature threshold within the infrared camera view of the central column. One pixel corresponds to an area of $\approx 3.6$ mm$^2$, and the camera view covers approximately 12.5% of the toroidal extent of the central column. Benign RE beam termination corresponds to large wetted areas, achieved at intermediate neutral pressures. Reproduced from [33]. © The Author(s). Published by IOP Publishing Ltd. CC BY 4.0.

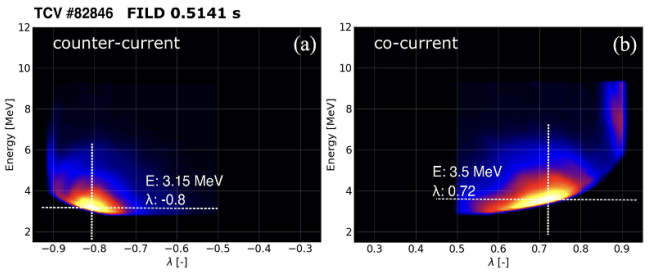


**Figure 5.** First-time, direct velocity-space resolved measurements of RE electrons moving in the (*a*) counter-current (passing REs) and (*b*) co-current (trapped and passing REs) direction, obtained with TCV's FILD diagnostic. $\lambda$ denotes the RE pitch, defined as the ratio of the velocity component parallel to the magnetic field to the total velocity. Reproduced from [39]. © 2025 The Author(s). Published by IOP Publishing Ltd on behalf of the IAEA. CC BY 4.0.

Velocity space mapping with this novel approach revealed both counter-current (passing) and co-current (trapped and passing) REs with energies in the range 3 MeV $< E <$ 6 MeV and pitch values $\lambda$ of $-0.90 < \lambda < -0.75$ and $0.55 < \lambda < 0.80$, respectively, figure 5. Here, $\lambda = v_\parallel / v$, where $v_\parallel$ is the RE velocity component along the magnetic field (positive if co-current) and $v$ is the magnitude of the total velocity. Spectrograms of the FILD signal and their correlation with fast magnetic measurements further point to interaction and transport of REs with low-frequency plasma instabilities.

## 4. AEs and FI physics

AE and FI studies have greatly advanced on TCV, supported by improvements in NBI [4] and diagnostic capabilities [40–46]. Scenarios with unstable AEs were developed in counter NBI plasmas, showing an increase in $T_i$ and no degradation of confinement time despite increasing NBI power, possibly related to AE-triggered zonal flows [47]. Flux-tube gyrokinetic simulations highlighted the need for a global approach on TCV due to the coupling of AEs and TEM turbulence and the development of radially elongated streamers. NBI-generated FIs were also shown to destabilise energetic particle driven geodesic acoustic modes (EGAMs) at sufficiently high fast particle pressure and low $q$, and the EGAM's detailed structure and non-rotating character was identified using multichannel SXR and AXUV diagnostics [48].

Systematic studies on the efficiency of ECRH and ECCD to stabilise AEs and the FI losses associated with AEs received particular attention [50]. On-axis ECRH demonstrated robust stabilisation of counter-NBI driven AEs when the ECRH deposition overlapped the mode location, albeit requiring significant input power (∼1.5MW of gyrotron power). On-axis counter-current ECCD also enabled effective AE suppression, while co-current drive showed AE mitigation. Suppression and mitigation mechanisms involved not only shear profile modifications, but also significant changes in plasma density and temperature, with the respective roles of these mechanisms yet to be quantified.

FI loss dynamics have been studied extensively, due to their risk of reducing heating efficiency and damaging plasma-facing components in future reactors. As a key diagnostic to probe FI losses, a unique FILD system has been designed, manufactured, and commissioned on TCV [40, 41]. It allows simultaneously measuring the co- and counter-current FI losses in forward and reverse magnetic field and is sensitive to both positively and negatively (see section 3) charged particles across the complete range of operational conditions. It features a two-camera system: a CMOS camera offering high-spatial resolution with medium-temporal resolution and a APD array providing medium-spatial resolution (sufficient for velocity space mapping) with high, MHz temporal resolution. Combined with a new version of the FILDSIM code [42], this system enables high-quality velocity-space sensitive FI reconstructions.

FI loss studies in low-collisionality peeling-limited [51] and high-collisionality IBL-like [49] scenarios revealed distinct inter- and intra-ELM FI transport. Significant inter-ELM FI losses were identified and linked to AEs and NTMs, respectively, in these regimes. The first-time, microsecond, velocity-space (energy E and pitch $\lambda$) resolved FI loss measurements allowed to recover the filamentary and burst-like velocity-space dynamics of the FI losses, exhibiting different pitch and energy values before, during and after the ELM onset. Some of these dynamics are apparent in figure 6 for the IBL-like scenario. In figures 6(*a*) and (*b*), magnetic fluctuations of a

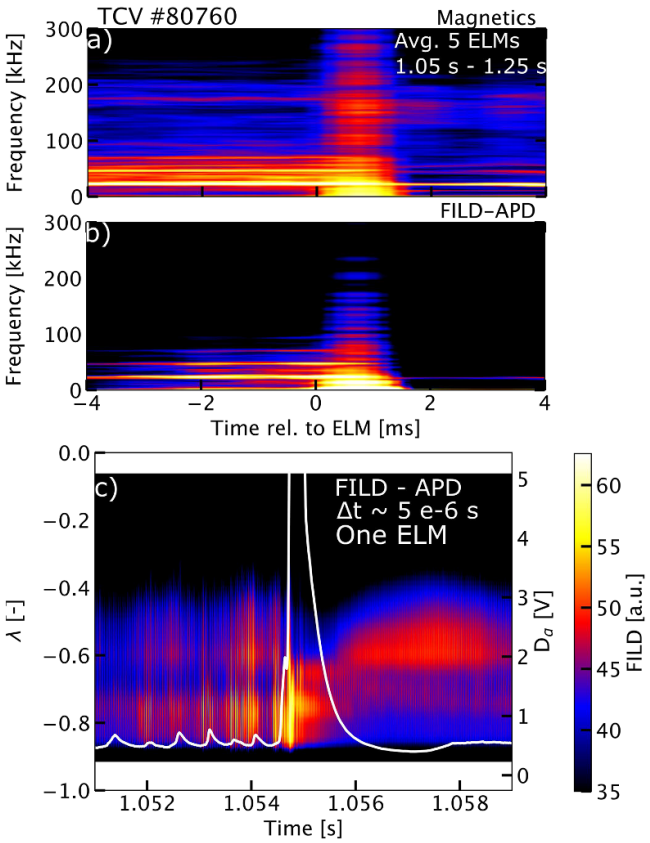


**Figure 6.** Inter- and intra-ELM FI loss study results, here for an IBL-like scenario. (*a*)–(*b*): ELM-synchronised data of the magnetic and the FILD spectrogram, averaged over 5 ELMs. (*c*): First-time, microsecond, velocity-space resolved FI loss measurement, here for the FI pitch, during a single ELM. The ELM $D_\alpha$ trace is overlayed in white. Reproduced from [49]. 

$m/n = 2/1$ NTM at ∼25 kHz and its harmonics are clearly visible also in the FILD signal, highlighting the associated FI losses. Instead, the higher-frequency magnetic fluctuations did not significantly contribute to the FILD signal and thus the FI losses. During the ELM, the FILD signal is characterised by a broadband spectrum, with the 25 kHz mode still present. The pitch-space mapped signal in figure 6(*c*) of a single ELM reveals strong loss levels in the vicinity of $\lambda = -0.6$ and $-0.8$. During the pre-ELM phase, these two pitch regions are clearly visible and show a discontinuous behaviour. During the ELM-crash, the loss population at $\lambda = -0.6$ vanishes and that at $\lambda = -0.8$ dominates. According to ASCOT5 orbit-following simulations [49], the losses at $\lambda = -0.6$ are associated with neoclassical losses while the losses at $\lambda = -0.8$ are associated with anomalous transport linked to the low-frequency MHD activity, and peaked during the ELM crash.

Both high-collisionality IBL and low-collisionality peeling-limited scenarios showed significant FI acceleration during the ELM crash [49, 51], resulting in FI energies exceeding the NBI energy by approximately a factor 1.5. This acceleration was observed in a narrow pitch region, implying a velocity-space dependent mechanism, typical of wave-particle interaction phenomena, which are yet to be identified. The FI acceleration has also been decorrelated from the ELM crash, contrary to previous studies and in line with recent AUG observations.

Finally, FI loss studies were also performed in plasmas with different triangularity. Studies in MHD-quiescent, limited NT and PT plasmas—both experimental and supported by ASCOT5 modelling—suggest, after carefully accounting for the different effects at play, that NT plasmas exhibit FI confinement levels similar to those of PT plasmas with the main difference arising from the orbit trajectories [52].

Moving forward, FI studies on TCV will benefit from further recent diagnostic developments [43–46]. In particular, an Ion Cyclotron Emission (ICE) diagnostic has recently been installed on TCV [44, 45]. This system—consisting of two orthogonally oriented B-dot probes mounted behind TCV wall tiles and coupled to a 1 GHz-frequency acquisition system—has enabled the first observations of ICE on TCV. Studies conducted in plasmas with ECRH heating and with co- and counter-current NBI revealed high-frequency oscillations driven by FIs as well as by thermal plasma populations, most prominently at harmonics of the core deuterium ion cyclotron frequency. This new diagnostic extends the suite of energetic-particle diagnostics, complementing in particular the FIDA (fast-ion $D_\alpha$) [46] and FILD systems used to probe FI dynamics. A planned expanded future array of ICE detectors will further allow for the direct determination of mode number and mode structure.

## 5. Core physics

On the path towards improved understanding and modelling of core turbulence, isotope effects on core transport were investigated in L-mode deuterium and hydrogen plasmas on TCV [53]. Increasing plasma density led to a transition from the Linear Ohmic Confinement (LOC) to the Saturated Ohmic Confinement (SOC) regime, occurring at higher density in D than in H. In the LOC regime, core transport was nearly identical for the two isotopes. In the SOC regime, instead, global energy confinement was higher in D plasmas, linked to reduced ion heat and particle diffusivities. These observations were largely reproduced qualitatively by local flux-tube gyrokinetic simulations with GENE, which identified collisionality-induced stabilisation as the main mechanism behind the reduced heat diffusivity in D. However, trying to achieve quantitative agreement pointed to missing physics in the simulations, such as electron-scale turbulence.

In terms of intrinsic core rotation generation—a key topic for predicting and optimising reactor-scale plasma performance—TCV's anti-collinear NBIs have been leveraged. For this purpose, previous studies of intrinsic rotation, driven by up-down asymmetric equilibrium shapes in Ohmic plasmas on TCV, have been extended to NBI-heated L-modes, quantifying intrinsic torque via balanced NBI experiments using co- (NBI-2) and counter- (NBI-1) injection [54]. Intrinsic torque was found to be in the counter-current direction in the plasma core, while the edge region exhibited significant co-current contributions. Up-down asymmetry-induced

intrinsic torque, estimated from non-linear GENE simulations, was of similar magnitude as inferred from experiments, but did not fully account for the observations, indicating the presence of additional torque sources and warranting further study.

Recent TCV core studies further benefited greatly from improvements in integrated modelling and diagnostic capabilities. Integrated modelling focused specifically on the ramp-up phase in Ohmic plasmas [55]. This modeling was performed with the High-Fidelity Pulse Simulator (HFPS), a Python workflow based on the IMASsified version of JINTRAC, self-consistently predicting current density, carbon impurity density, as well as $T_e$, $T_i$, and $n_e$. The electrostatic code QuaLiKiz and the fluid code TGLF, used to calculate turbulent fluxes, predicted a transition from TEM early in the discharge to ITG dominated turbulence. Good overall agreement was reached between integrated modelling and experimental data, and the predicted turbulent fluxes showed qualitative agreement with the higher fidelity model GKW. Extensive sensitivity tests performed for these discharges indicated the important role of the initial conditions of the $q$ profile and of $Z_{\text{eff}}$ on the simulation outputs [55]. Applying the developed pipeline to a larger number of discharges and to different devices would furthermore allow for a more comprehensive validation.

For improved reconstruction of plasma magnetic equilibrium and profiles, a workflow was proposed and tested on TCV [56], coupling the equilibrium reconstruction code LIUQE with the dynamic state observer RAPTOR [57]. In addition to the profile evolutions of the poloidal flux $\psi$, $T_e$, and $n_e$, the workflow provides estimates of further physical quantities such as the effective charge $Z_{\text{eff}}$, the on-axis ion-to-electron temperature ratio, and an improved safety-factor profile. It also enables improved kinetic equilibrium reconstruction, capturing in particular the sharp gradients in the H-mode pedestal region. Beyond its use in post-discharge analysis, integration of this approach into the TCV control system (section 8) for model-based, real-time plasma-state reconstruction is currently underway.

In terms of improved tomographic reconstruction techniques, a unifying perspective on sparse-view tomography has been developed and interpreted within a Bayesian framework [58]. A robust linear stochastic gradient flow algorithm, applied to the inferred posterior distribution, was shown to yield credible tomographic reconstructions together with associated uncertainty quantification. As a first application, the method was tested on the TCV soft x-ray system using a large dataset of model phantoms, thereby validating the approach while also highlighting intrinsic challenges of sparse-view tomography.

Moving closer towards the edge, the capability of TCV's short-pulse reflectometry (SPR) system to measure turbulence amplitudes in the plasma outer-core region has been validated using a new synthetic diagnostic, based on local gyrokinetic GENE simulations coupled with the full-wave CUWA code [59]. These SPR capabilities made it possible to confirm reduced relative density-fluctuation levels in NT compared with PT plasmas, while revealing similar radial correlation lengths. With the help of Machine Learning methods, the applicability regime of the SPR could be extended to higher turbulence amplitudes than those accessible by traditional reflectometry methods [60]. Together with major hardware upgrades [61], the SPR system now further delivers 20-point outer core/edge density profiles every 400 ns, and allows for detailed studies of fast transient phenomena such as edge-localised modes.

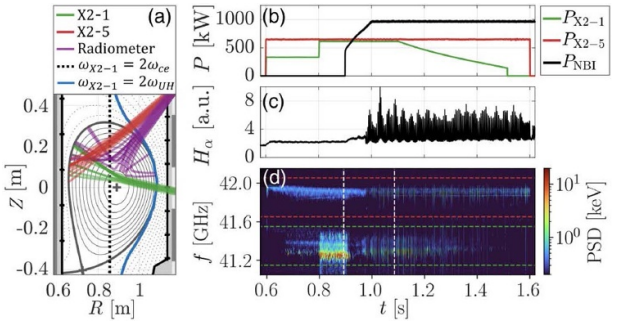


**Figure 7.** (*a*) Poloidal cross section of a TCV discharge with resonances, gyrotron ray trajectories, and line of sight of the radiometer overlayed. (*b*) and (*c*) Time traces of the injected power and $H_\alpha$ signal, with the latter highlighting the transition to H-mode following NBI injection. (*d*) Frequency spectrum of the radiometer, showing a clear signal at half frequency of both the X2-1 gyrotron (41.35 GHz, indicated by the green band) and the X2-5 gyrotron (41.90 GHz, indicated by the red band) as a result of a Two-Plasmon Decay Instability (TPDI), with different characteristics in the L-mode and H-mode phases of the shot. Reprinted figure with permission from [64], Copyright (2024) by the American Physical Society.

For the remainder of this section, we focus on studies of electron cyclotron (EC) wave propagation and related diagnostic methods, where substantial progress has been achieved. On TCV, suprathermal electron distributions resulting from EC wave absorption are typically broader than theoretically predicted. The hypothesis that broadening of EC beams due to scattering from turbulent density structures in the plasma edge could account for this discrepancy was investigated [62]. Full-wave modelling of LFS-launched X2 waves, incorporating experimentally inferred edge density fluctuation levels, indicated that the simulated beam broadening remained insufficient to explain the measurements. This suggests that, at least for the configurations studied, additional broadening mechanisms were at play [63].

Further insights on the interaction and result of X2 beams and plasma turbulence were obtained with radiometer measurements on TCV [64]. These measurements revealed that Two-Plasmon Decay Instabilities (TPDIs) occur regularly in the TCV edge during X2 microwave injection in both L- and H-mode, see figure 7. TPDIs are a class of parametric instabilities, where the gyrotron beam decays nonlinearly into two electron Bernstein waves (EBWs) with approximately half of the original frequency. They are caused by trapping of the EBWs in edge density fluctuations created by blobs or ELMs and saturate through subsequent decays into up- and down-shifted EBWs. The subsequent decays indicate a generation of high-harmonic ion Bernstein waves, which is supported by an observed correlation with FI production. Together with the work in [62], these findings clearly highlighted the importance

of non-linear microwave propagation effects in view of ITER and DEMO, and could potentially be used on ECRH devices as a diagnostic for density fluctuations in the plasma edge or for concave density fluctuations in the confined plasma, e.g. due to rotating islands [65].

Staying within the domain of EC-wave physics, vertical electron cyclotron emission (V-ECE) measurements of non-thermal electrons were obtained for the first time on TCV [66, 67]. This was made possible by overcoming previous limitations of this approach, related to thermal background radiation, by tuning the toroidal magnetic field and carefully selecting the ECE spectrum. This provided information on the non-thermal electron distribution in scenarios with ECCD and REs. In the ECCD case, an increase in the number of suprathermal electrons was observed in both the parallel and perpendicular directions, whereas in the RE case the increase appeared mainly in the parallel direction. These results potentially open the way to a renewed use of ECE as a diagnostic for fast electrons in tokamaks.

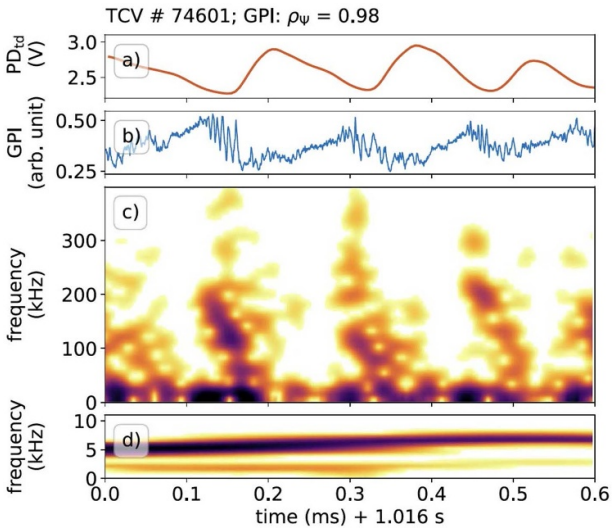


**Figure 8.** Insights on the dynamics in the I-phase: a high-frequency mode is clearly identified in the high-bandwidth GPI signal, (*b*)–(*c*), acting as a precursor to the bursts (LCOs) visible in the photodiode (PD) signal in (*a*). Reproduced from [73]. © 2024 The Author(s). Published by IOP Publishing Ltd on behalf of the IAEA. CC BY 4.0.

## 6. Edge/pedestal physics

New insights on plasma edge/pedestal physics on TCV were enabled by a new Doppler backscattering (DBS) system, installed to probe edge poloidal velocities ($v_\perp$), radial electric field ($E_r$) profiles, and associated fluctuations in the upper low-field side region of the plasma [68]. The measured $v_\perp$ profiles were found to agree with Gas Puff Imaging (GPI) measurements in the overlapping region, and the inferred $E_r$ was consistent with radial force balance evaluations using $C^{6+}$. Edge $v_\perp$ radial profiles were studied across L-mode scans in density, auxiliary heating, and magnetic field helicity. Co-current NBI consistently increased $v_\perp$ in both limited and diverted configurations, in qualitative agreement with the expected response to toroidal torque, while ECRH had only a modest effect. In diverted plasmas, the $v_\perp$ profile and the related $E_r$ well showed moderate variation with density and NBI, and no variation with changing helicity. Interestingly, however, the velocity shear kept increasing with increasing NBI power at the inner side of the $E_r$ well, emphasising the inner-well shear's role in the L–H transition. The first edge $E_r$ measurements in TCV NT plasmas further revealed deeper $E_r$ wells in Ohmic, NBI-heated, and ECRH-heated NT discharges compared with their PT counterparts [69]. These results suggest a causal link between $E \times B$ shear and improved confinement, in line with the turbulence suppression paradigm by sheared flows.

In terms of edge/pedestal fluctuation studies, the first gyrokinetic GENE simulations of the TCV pedestal were carried out in the pre-ELM phase of 170 kA, 1.1 MW NBI H-mode plasmas at two different levels of gas puffing, aimed at determining the role of electron temperature gradient (ETG) modes in pedestal transport [70]. These local, electron scale simulations showed that at low gas puffing, electron heat fluxes due to ETGs are negligible compared to the total experimental electron heat flux. At high gas puffing, instead, ETG-driven electron heat fluxes matched experimental values, suggesting that ETG modes become the limiting factor for pedestal formation. These simulations also highlighted the importance of toroidal-ETG, rather than slab-ETG, in these high gas puffing conditions.

Experimentally, inter-ELM edge fluctuations have been investigated with the Thermal Helium Beam (THB) diagnostic [71], across a relatively large dataset of NBI and ECRH heated Type-I ELMy H-modes [72]. These discharges featured low gas puffing, plasma currents of 160 kA and 240 kA, and differed primarily in the amount of injected ECRH power. Coherent, inter-ELM fluctuations were identified around the separatrix, in the range of 30–90 kHz. They appeared a few hundred microseconds after the ELM and showed a continuous frequency decrease before disappearing 0.3–0.5 ms prior to the next ELM crash. These fluctuations were primarily visible in electron density, without a clear signature in electron temperature. The frequency decrease correlated with a steepening of the pedestal density profile during the ELM cycle and, across discharges, showed a positive correlation with the injected heating power.

Edge fluctuations were also investigated in the I-phase, an H-mode confinement regime characterised by so-called limit cycle oscillations (LCOs) or bursts that periodically flatten the plasma edge profiles [73]. Beyond its intrinsic interest, the I-phase is significant because of the proposed connection between LCOs and Type-III ELMs. Using GPI, the I-phase was identified unambiguously on TCV for the first time, and its distinction from L- and H-mode dithers was clearly demonstrated. A high-frequency edge mode (100–200 kHz) was observed as a precursor to the LCOs and the associated profile flattening, see. figure 8. This flattening was accompanied by bursty filamentary transport in the SOL, as detailed in 2D with GPI.

## 7. SOL and divertor physics

SOL/divertor and exhaust studies advanced substantially on TCV, supported by improved diagnostic techniques, advanced modelling, and systematic experimental studies in conventional and alternative divertor geometries—with the removable divertor baffles remaining a central element.

### *7.1. Improved divertor diagnosis, including ion temperatures and flows*

Long outer divertor leg scenarios were extensively used to maximise diagnostic coverage of the divertor. Detailed measurements from existing diagnostics, including 2D maps of $T_e$ and $n_e$ from Divertor Thomson Scattering (DTS) achieved via outer leg sweeping, were complemented with new measurement capabilities of the Divertor Spectroscopy System (DSS) [75], the novel Tangential DSS (TDSS) [74], and improved neutral pressure measurement capabilities [76]. Divertor $T_i$ profiles were inferred with the DSS from Doppler broadening of C II, C III, and He II emission lines, in conditions ranging from strongly attached towards detached conditions [75]. These line-of-sight-integrated and emission-weighted measurements were compared to corresponding emission-weighted DTS electron temperature data and interpreted with a model for the divertor $T_i$ evolution. This model includes the ionisation state evolution of the impurities and the coupling to the main plasma and neutral species. It predicts that the $C^{2+}$ and $He^+$ ion temperatures closely follow the main-ion temperature and reproduces the relative differences and agreements between measured ion temperatures and $T_e$ in different divertor locations and regimes. While collisional coupling between the different species was found to be important in the divertor, upstream $T_i$ and $T_e$ measurements from Charge Exchange Recombination Spectroscopy (CXRS) and TS showed that ion and electron coupling plays a minor role in the edge plasma [77]. Instead, the upstream $T_i/T_e$ ratio was found to mainly depend on the relative ion and electron heat fluxes from the core.

Additional diagnostic coverage of the long leg scenario was obtained with the TDSS, which measures spatially resolved divertor ion temperatures and parallel (to the magnetic field) velocities ($V_i$) for species such as $C^{2+}$, $N^+$, and $He^+$ [74]. The system operates in both the near and far divertor SOL and across a wide range of magnetic configurations. Some representative data for $C^{2+}$ is displayed in figure 9. In this same scenario, $D^+$ Mach numbers, inferred from the TDSS, were found to agree with Mach probe measurements from the Reciprocating Divertor Probe Array (RDPA). These divertor flow measurement capabilities were further complemented with an improved coherence imaging spectroscopy (CIS) system with a polarisation-sensitive sensor, enabling 2D, line-integrated flow measurements [78]. This system provides higher velocity accuracy and spatial resolution than previous systems and initial divertor flow measurements of $C^+$ identified a strong velocity gradients across the divertor leg, to be further investigated.

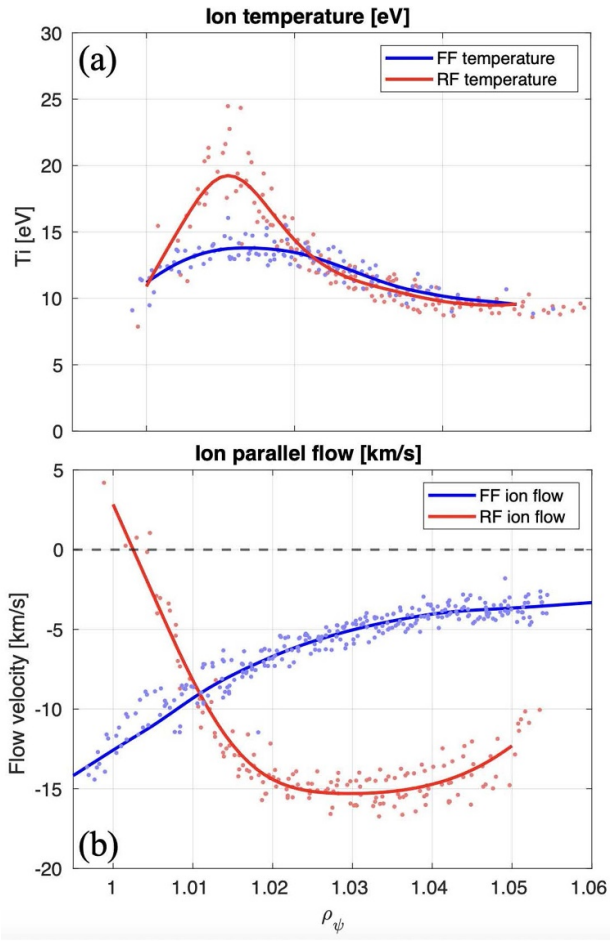


**Figure 9.** Radial profiles of the $C^{2+}$ ion temperature and parallel flow velocity in the divertor at $Z = -0.46$ m (corresponding to a height of 0.29 m above the TCV floor tiles) for a long-leg scenario (see text), for both forward and reversed toroidal field directions and obtained with the TDSS [74]. Data points represent raw measurements derived from Doppler broadening and Doppler shift of the emission line, while the lines show spline fits to the data. Negative flow velocities correspond to flows directed towards the outer target.

### *7.2. Modelling and model validation*

The work discussed in section 7.1, as well as related studies, combined with progress in divertor transport code simulations, helped to elucidate various aspects of divertor physics and to validate the numerical tools. SOLPS-ITER simulations of the TCV divertor and comparison with experiments identified a strong underprediction of molecular-related processes. This discrepancy was largely reconciled by using corrected molecular charge-exchange rates [79], which led, among other effects, to a strong increase in the divertor $D_2^+$ density, a 60% increase in hydrogenic power losses due to molecular activated dissociation (MAD), and the reproduction of the ion target flux roll-over through enhanced molecular activated recombination (MAR). Molecular divertor spectroscopy further identified a significant increase of the rotational $D_2$ temperature during detachment and associated further divertor power and momentum losses, highlighting the impact of ion–molecule collisions [80].

Combining dedicated experiments and SOLPS-ITER simulations of TCV L-mode plasmas demonstrated synergistic benefits of impurity seeding and divertor baffling [81]. With baffles, divertor deuterium neutral density and compression increased. This increase was attributed to reduced neutral conductance between the divertor and main chamber, as quantified with a schematic neutral transport model. For a given seeding rate, baffling also strongly enhanced the divertor compression of neutral nitrogen. In contrast, the compression increase of nitrogen ions was less clear, and depended on changes in main-ion flows and ion temperature induced by baffling and seeding. While baffling still provided significantly improved divertor cooling for a given seeding rate, this study highlighted the importance of advancing and validating divertor impurity transport models, a key ongoing effort.

The effect of baffles and nitrogen seeding was also investigated with SOLEDGE3X-EIRENE, focusing on TCV H-mode plasmas [82]. The simulations showed that for both short and long outer baffles, divertor detachment occurred at similar values of divertor neutral pressure, while nitrogen reduced the target temperature with little effect on the upstream plasma density and momentum loss but dropped the upstream pressure. These simulation results were compared to an empirical partial detachment qualifier, calibrated previously on AUG, showing promising agreement.

SOLPS-ITER simulations were further challenged through validation against extensive experimental datasets. The near-sheath-limited, diverted L-mode reference case TCV-X21, originally developed for validating boundary turbulence codes, served as a benchmark. In addition, its comprehensive, publicly available dataset was extended to include neutral-related observables [83]. In a proof-of-principle approach, key input parameters (fuelling rate, particle diffusivity, and heat diffusivity) were optimised using a quantitative experiment-simulation agreement metric, and the resulting outputs were then compared with experimental measurements. While good agreement was generally obtained upstream and at the divertor entrance, discrepancies remained in the divertor region, partly attributable to the absence of drifts in the simulations. Previously identified disagreements in divertor flows between GBS turbulence simulations and experimental RDPA data could not be resolved, with SOLPS-ITER providing intermediate results, thereby motivating further studies. SOLPS-ITER validation efforts have also focused on dissipative divertor scenarios, with and without divertor baffles [84]. Earlier simulations predicted overly dense and cold divertor target conditions. Subsequent improvements, most notably in the treatment of ion flux limiters and carbon sources, led to significantly better agreement with experiment, figure 10. Additional progress in core-edge coupling was obtained by including a convective transport contribution, motivated by JINTRAC.

SOL/divertor modelling on TCV also progressed with 1D codes, providing an important intermediate step between simplified analytical models and the more realistic, but also more complex, 2D and 3D approaches. A new 1D code, SPLEND1D, was introduced and described in detail [85]. It solves the Braginskii equations along the magnetic field, coupled to a fluid neutral model. The code is fast and versatile,

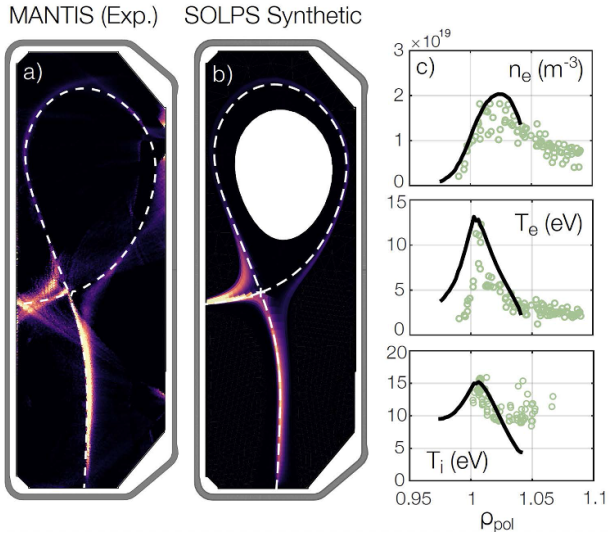


**Figure 10.** Comparison of SOLPS-ITER outputs with experimental data for quantities that were previously poorly reproduced. (*a*) and (*b*): measured and simulated C III emissivity distributions. (*c*): radial profiles of electron density and temperature from TS and ion temperature from TDSS, taken halfway down the outer divertor leg (green markers), compared with the corresponding SOLPS-ITER results (solid black lines). Reproduced from [84]. 

allowing variation of magnetic pitch angle and field strength, as well as time-dependent simulations. Initial studies qualitatively reproduced detachment in TCV-relevant conditions and provided insights into the roles of divertor connection length and flows in the detachment process.

To reduce the gap between fast 1D models and advanced 2D transport simulations, another 1D SOL solver, DIV1D, was benchmarked against 1D-mapped SOLPS-ITER data [86]. By calibrating scenario- and device-specific input parameters (SOL width, core ionisation fraction, and neutral exchange velocity), DIV1D reproduced SOLPS-ITER predictions of heat flux, $T_e$, and $n_e$ along the main heat-flux channel, from upstream to target, within about 50%.

Finally, moving from 1D to 0D models and motivated by the need to ensure reliable plasma startup scenarios in future fusion devices, the classical 0D Townsend breakdown theory was experimentally validated on TCV [87] over a wide range of breakdown parameters. The theory was found to be surprisingly accurate, correctly predicting the occurrence of breakdown within 1 $\sigma$ error bars in over 95% of the cases when a threshold of 8–13 ionising collisions per connection length is met. The study also demonstrated for the first time that the gradient of the poloidal magnetic-field null is a critical control parameter: a smaller gradient significantly increases the effective electron connection length, thereby reducing the loop voltage required to initiate the plasma.

### *7.3. Alternative divertor studies*

The investigation of alternative divertor configurations (ADCs) [88] has continued to be a central theme on TCV,

offering a promising route to optimise exhaust handling in DEMO and likely constituting a necessity for the high-field, compact fusion approach. The individual roles of key geometric divertor parameters in power exhaust have been thoroughly revisited, supported by enhanced diagnostic capabilities, improved theoretical understanding, and the recent ability to routinely obtain SOLPS-ITER simulations of TCV plasmas—including drifts—with orders-of-magnitude improvement in convergence speed [89].

In systematic L-mode density scans, the impact of poloidal and total flux expansion, the key features of the X-Divertor (XD) and the Super-X Divertor (SXD), on the detachment threshold were shown to be smaller on TCV than expected from simple analytical models [90]. Substantially larger improvements were obtained from extending the outer divertor leg length. These results compare favourably with SOLPS-ITER simulations and elucidated the role of plasma drifts, parallel flows, and power and momentum losses in reproducing the experiments—effects that are typically neglected or only partially included in analytical models.

Strong power exhaust benefits were demonstrated in the X-Point Target (XPT) divertor geometry, which incorporates a secondary X-point located near the divertor target. Experiments on TCV revealed a novel XPR regime, the X-point target radiator (XPTR), that forms at this secondary X-point [91], figure 11. Unlike the conventional XPR regime discussed in section 2, the XPTR spatially decouples the radiator from the confined plasma. This points to a new class of power exhaust concepts that allow divertor detachment without radiative edge cooling, with promising implications for core-edge integration and reduced proximity to operational limits. In the Ohmic XPT plasma studied in [91], detachment was accessed far more readily than in standard single-null (SN) configurations, with divertor target heat fluxes reduced by more than a factor of five. This was accompanied by the emergence of a stable, localised radiative zone around the secondary X-point, whose position showed remarkable insensitivity to upstream density variations—an increase in robustness exceeding a factor of five compared to the SN case. Enhanced detachment front position resilience against fuelling, seeding, and heating perturbations was further demonstrated at dynamic timescales, which is key in view of facilitating real-time detachment control [92].

First SOLPS-ITER simulations of TCV XPT plasmas, with drifts included, identified a convective cell in the vicinity of the secondary X-point and highlighted the important role of the associated $E \times B$ drift in determining density and temperature profiles at the active strikepoints [90].

Following the initial demonstration of the XPTR, its superior exhaust performance has also been confirmed in scenarios with significant second-harmonic ECRH (2.5 MW), with values of the detachment accessibility metric $PB/R/n_{\mathrm{sep}}^2$ comparable to that predicted for SPARC reference scenarios [93]. In this expression, $P$ is the power crossing the separatrix, $B$ the on-axis magnetic field, $R$ the on-axis major radius, and $n_{\mathrm{sep}}$ the upstream separatrix density. While, according to CIII from

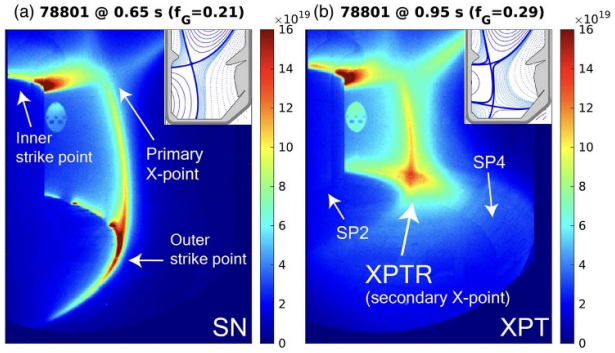


**Figure 11.** $D_\alpha$ filtered images showing the XPTR development during the transition from (*a*) SN to (*b*) XPT. Insets show the magnetic equilibria. Reprinted figure with permission from [91], Copyright (2025) by the American Physical Society.

measurements, nitrogen seeding in this scenario did not lead to detachment in SN, it triggered early XPTR onset and associated detachment in the XPT. Extended to Type-I ELMy H-mode, XPT operation also showed strong indications of passive mitigation of large transient heat loads caused by ELMs [94], which could substantially increase the maximum allowed ELM size in future reactors. Assessing how these results scale to larger devices and reactor-like power levels will, however, require further investigation. High-fidelity modelling provides a key tool to address this issue and constitutes a core element of ongoing work [90].

Since most ADC concepts primarily enhance the exhaust performance of the outer divertor, they can naturally be combined with up-down symmetric Double-Null (DN) configurations featuring two active outer divertor strike points. This provided additional motivation to focus on DN physics. An analytic scaling law for up-down power sharing in DN L-mode was derived from first-principles modelling with the GBS code and validated against TCV experiments [95]. This model highlighted turbulence, diamagnetic drifts and geometric imbalance as the main asymmetry drivers. The in-out power sharing in DN was experimentally shown to depend on triangularity, with the power fraction to the inner target approximately doubling when reducing triangularity from 0.58 to 0.17 [96]. This effect was ascribed to a reduction of poloidally ballooned radial transport and enhanced cross-field transport through the high-field side separatrix.

### *7.4. Divertor turbulence studies*

The interplay of turbulence and kinetic neutrals in the detachment process was studied using GBS turbulence simulations based on high-density TCV L-mode plasmas [97]. The simulations included three plasma species (electrons, $D^+$, and $D_2^+$) coupled to two kinetic neutral species (D, $D_2$), and led to detachment of the inner divertor target at high levels of gas puffing. An assessment of the different collision terms highlighted the crucial role of molecular interactions in the detachment process. These simulations further revealed an increase in the near-SOL density and pressure decay lengths, as well

as the formation of a density shoulder, at high gas puffing, consistent with experimental observations. This behaviour was attributed to reduced parallel transport together with enhanced radial transport, associated with larger and faster blobs.

A direct, quantitative comparison of key blob properties simulated with GBS and measured with GPI was carried out in the near-sheath-limited TCV-X21 reference case, using a dedicated synthetic GPI diagnostic [98]. Poloidal and radial blob velocities at the outboard midplane and in the divertor region were found to be in quantitative agreement between simulation and experiment. However, the code overestimated blob radial and poloidal sizes by approximately a factor of two, providing stringent constraints for future simulation improvements. In reverse magnetic field scenarios, both experiment and simulation revealed a poloidal blob motion opposite to the background poloidal $E \times B$ drift in the divertor leg. The simulations explained this behaviour by strong changes in the instantaneous $E \times B$ drift associated with blobs, rather than by effects related to parallel transport.

The relative importance of divertor and outboard midplane fluctuation-induced radial particle fluxes has been investigated with fast reciprocating probe measurements in L-mode discharges of varying collisionality and divertor geometry [99]. Both at low and high collisionality, within one power fall-off length of the separatrix, the radial particle flux in the divertor was found to be small—only about 20% of that at the outboard midplane. Fluctuation characteristics were found to be consistent with a resistive X-point turbulence regime, with a possible transition to a resistive ballooning regime at high density. Interestingly, in the inter-null region of the Snowflake divertor, where increased cross-field transport is often predicted, a reduction of up to 50% compared to the SN geometry was observed. A follow-up study [100] specifically investigated conditions at detachment onset. Results showed that upstream density profile broadening in these conditions was associated with a 2- to 4-fold increase in the fluctuation-induced radial particle flux in the vicinity of the X-point and further upstream. In contrast, radial transport downstream of the dissipative region remained at levels similar to those in attached conditions.

## 8. Control

TCV's flexible, digital, distributed control system underwent major hardware and software upgrades and, after years of development, evolved from an experimental setup into a stable and reliable platform [102]. This system, called SCD (in French Système de Contrôle Distribué), is based on three pillars: MATLAB Simulink, the MARTe2 real-time control framework, and MDSplus. The SCD controls, in real time, TCV's 20 independent coil power supplies, 13 gas injection valves, multiple steerable EC launchers, and two NBIs and several gyrotrons with continuously adjustable power. Most legacy real-time codes, such as magnetic reconstructions, MHD mode analysis, the RAPTOR current density and electron temperature observer and the RAPDENS electron density observer, have already been ported to the new framework. Increasingly, the SCD also integrates real-time capable diagnostics, a trend further strengthened by the recent inclusion of the Data Distribution Service (DDS) [103]. These diagnostics currently include 117 Thomson Scattering lines of sight, 10 filtered camera images (MANTIS), 14 far-infrared interferometry chords (FIR), 64 fast magnetic probes, and 120 bolometry lines of sight (RADCAM).

The SCD combines the flexibility needed for rapid prototyping and the rigour required for long-term algorithm maintenance. As detailed in this section, it has been central to the substantial progress achieved over the past two years in nearly all aspects of tokamak control—from breakdown and ramp-up, through flat-top operation and off-normal event handling, to ramp-down.

In [104], a model-based plasma breakdown design was combined with a shot-to-shot correction algorithm based on Iterative Learning Control (ILC) to accelerate the development of robust plasma start-up. This strategy was successfully demonstrated on TCV, where it enabled rapid scenario adjustments and the achievement of the desired magnetic field configuration together with a stable plasma current ramp-up in feedforward mode within only a few iterations. The method represents a valuable tool not only for present-day tokamaks but also for the early operational phases of future devices such as ITER, where minimising the time required for reliable breakdown development will be crucial.

To improve vertical plasma control across all phases of the discharge, from start-up through flat-top to ramp-down, real-time estimates of the vertical instability growth rate were refined by accounting for the effects of radial displacements [105]. This opens the way to future integrated plasma control schemes where real-time vertical growth rates will be used to select the proper scenario in the spirit of minimising and, possibly, totally avoiding vertical displacement event (VDE) disruptions. In parallel, model-free, data-driven approaches for vertical control were also explored, notably with the recent adaptation of the Extremum Seeking-based Vertical Stabilisation control algorithm for TCV [106].

In terms of improved plasma shape control, a novel, real-time, model-based shape controller has been designed, implemented, and experimentally validated on TCV [101]. It controls the plasma shape through an isoflux approach with improved interpretability developed in [107]. This shape controller operates on top of the primary magnetic control, forming a nested control architecture, which limits its impact on machine operation and eased its deployment, figure 12(*a*). The controller was tested across a variety of plasma configurations and achieved significant improvements in plasma shape accuracy, as shown by the example in figure 12(*b*). The same nested control architecture has also been exploited to test a first-of-its-kind Model Predictive Controller for the plasma shape in TCV [108]. While similar solutions had been proposed in the literature for future devices such as ITER and DEMO, this is the first time that a Model Predictive Control (MPC)-based shape controller was deployed and successfully tested in real-time on a real tokamak device. In parallel, TCV's alternative magnetic control approach based on reinforcement learning

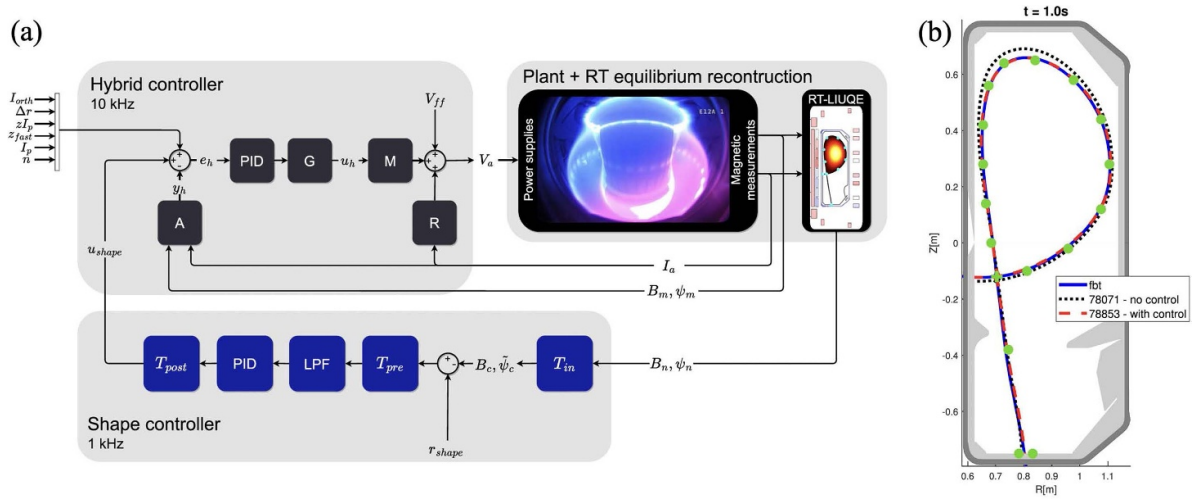


**Figure 12.** (*a*): Block diagram of the TCV magnetic control architecture. (*b*): Comparison of the programmed plasma boundary (solid blue) with discharge 78 071 without shape control (black dotted) and discharge 78 853 with shape control (red dashed) at $t = 1.0$ s. Reproduced from [101]. © The Author(s). Published by IOP Publishing Ltd. CC BY 4.0.

(RL) was further refined and improved [109]. Techniques were presented that address some key limitations, achieving notably reduced shape error and shorter training times. In addition, several promising directions for further improvement were identified.

An important aspect in plasma magnetic control is the avoidance of saturation of the currents in the poloidal field (PF) coils. In [110], the Current Limit Avoidance (CLA) system foreseen of the ITER Plasma Control System (PCS) was experimentally tested on the TCV tokamak, highlighting its suitability for future devices. An alternative CLA system was further tested in [111].

A key step in de-risking the operation of ITER and DEMO is the proof-of-principle testing of model-based observers, since these devices will operate with fewer diagnostics than current machines and under more stringent controllability requirements. In this context, improved estimation of the dynamic evolution of the electron density profile, critical for its monitoring and control, was demonstrated in TCV L- and H-mode plasmas [112, 113]. The approach relies on the RAPDENS observer, employing the Extended Kalman Filter (EKF) technique to incorporate in real time low-frequency Thomson scattering measurements and high-frequency, line-integrated interferometry measurements with a control-oriented model for the particle balance evolution in TCV. Beyond real-time profile reconstruction, fast transport solvers are also used on TCV to improve pre-shot pulse designs [114], using RAPTOR coupled to the Free-Boundary Tokamak (FBT) equilibrium code, as well as for post-shot kinetic-equilibrium reconstruction and physics-parameter estimation [56], as discussed in section 5.

Another key aspect for robust control is automatic, real-time labelling of confinement states, which was substantially advanced in [115] through data-driven models incorporating uncertainty quantification and robustness. Robust classification of L-mode, H-mode, and dithering phases was achieved, with resilience to missing or faulty diagnostic signals. Remaining challenges concern the precise timing of the transition, pointing to several promising directions for future work.

To obtain an interpretable representation of the plasma operational space with respect to disruption limits, a data-driven method was developed based on a Variational Autoencoder (VAE) architecture [116]. The model projects the plasma temporal evolution as continuous trajectories in a low-dimensional latent space, partitions the operational domain into distinct regimes, and estimates proximity to disruptions. Applied to a dataset of $\approx 1600$ TCV discharges, the method successfully distinguished different disruption types and enabled downstream analyses, such as automatically identifying combinations of parameters associated with disruptive events. Still on the topic of disruptions, H-mode density limit (HDL) disruption avoidance, based on direct measurements as well as state-space observers and using both continuous control and exception handling, was demonstrated and routinely implemented on TCV [117]. To test the transfer of disruption avoidance schemes between devices and their extrapolation to larger machines, TCV, AUG, and JET were used in a step-ladder approach. Experimental studies confirmed that the MARFE dynamics preceding the HDL were similar in all three devices, with the main difference being the associated timescales. These increased with device size, with beneficial implications for ITER and DEMO.

Significant efforts were also dedicated to controlling plasma–wall interactions in both the main chamber and the divertor. In collaboration with the ITER PCS design team, a real-time-capable plasma heat flux estimator for the ITER first wall was adapted to the TCV geometry and integrated into its digital control system. Leveraging the shared PCSSP [118]/SCDDS [102] technology enabled the rapid deployment of a prototype first wall heat load controller, implemented as an external loop to the TCV plasma shape controller and used to regulate the heat flux on the TCV central column through adjustments of the plasma radial position [119]. This work

represents a first example of comprehensive 'tokamak-in-the-loop' ITER-relevant experiments planned for TCV.

Turning to the divertor region, detachment control is now routinely performed on TCV in a variety of regimes. A recent development is the demonstration of divertor emission front control during strike-point sweeping [120], which is considered as a potential emergency solution for EU-DEMO in case of a loss of plasma detachment. For the design of robust detachment controllers on TCV and other devices, experimental evaluation of the divertor state's dynamic response to actuator actions—typically probed with periodic perturbations such as multi-sines—plays a central role. In [121], an extensive multi-device investigation of exhaust dynamics in response to deuterium fuelling, impurity seeding, and plasma heating was presented, covering data from TCV, MAST-U, ASDEX-Upgrade, WEST, DIII-D, and JET. The study showed in particular that the SOL equilibrates on fast time scales (well above 70 Hz) and that the divertor plasma response to gas valve modulations is predominantly linear and smooth, which explains the success of linear detachment controllers across devices. Variations were found to be remarkably small across scenarios (H-mode, L-mode), injection locations, and devices. This dataset provides extensive benchmarks for the validation of dynamical, physics-based heat exhaust and SOL models, which are essential for model-based designs of detachment controllers in future devices.

A series of such dynamic exhaust models were introduced and validated against TCV data in [122], focusing on the dynamic response of plasma and neutrals to deuterium gas puff modulations. Three models of varying fidelity were tested: a three-chamber model simulating 0D particle reservoirs, a model based on DIV1D, and time-dependent simulations with SOLEDGE3X-EIRENE. These studies showed that the dynamic behaviour of TCV in response to gas puff modulations can be reproduced with SOLEDGE3X-EIRENE, and also with the first two models for specific parameter settings. Connecting the neutral reservoir outside the plasma with both the SOL and the core plasma was found to be essential to reproduce the experimental behaviour.

In terms of related diagnostic improvements, tomographic inversions were made real-time capable in view of control applications. Using data from the MANTIS system, two neural network architectures were developed and trained on synthetic data, enabling tomographic inversions fast enough for real-time control [123].

Last but not least, the challenges associated with high disruptivities during plasma rampdowns were addressed in [124]. By combining physics-based equations with data-driven models and leveraging recent advances in Scientific Machine Learning, Neutral State-Space Models (NSSMs) were used to predict TCV plasma rampdown dynamics in a variety of experimental conditions. These NSSMs feature high sample efficiency, requiring only a modest amount of experimental data from TCV - 311 rampdowns in low-performance discharges and only five rampdowns in relevant high-performance conditions ($\beta_N > 2$ and near the density limit). The NSSMs can simulate a large number of rampdown trajectories ($\approx 10^4$ per second on a single A100 GPU), enabling the design of

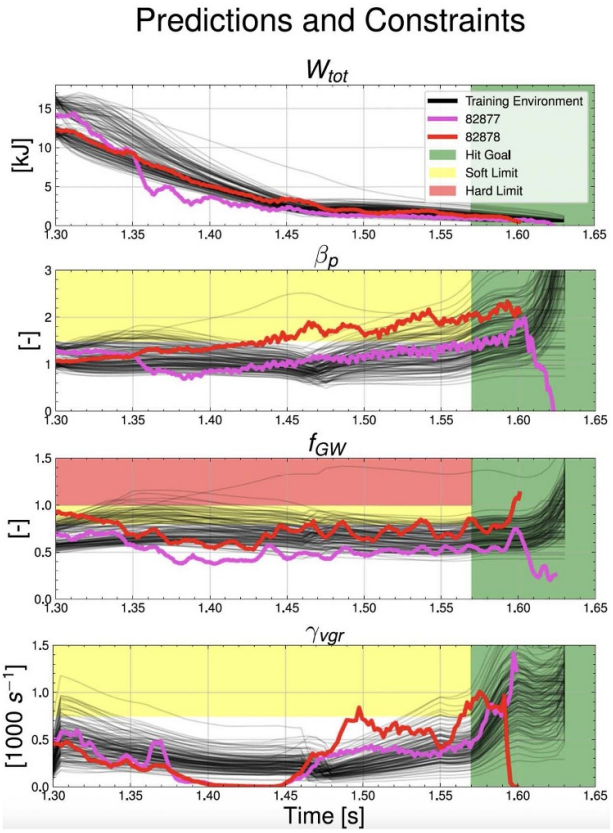


**Figure 13.** Predictions and experimental results of rampdown trajectories based on Scientific Machine Learning, for a high-performance discharge with plasma current extrapolation, demonstrating successful plasma termination. Shown are the experimental time traces of stored energy, plasma beta, Greenwald fraction, and vertical growth rate, together with the *a priori* predictions (black curves). Reproduced from [124]. 

robust rampdown trajectories using RL. After a small number of trial-and-error iterations, reliable plasma termination was demonstrated for five consecutive high-performance discharges. These also included small scenario extrapolations (increasing the plasma current from 140 kA to 170 kA), figure 13, mimicking the incremental scenario developments foreseen for future devices such as ITER and SPARC. These results constitute one of the first successful demonstrations of trajectory design with robustness to real-world uncertainties in tokamaks. Next steps, also discussed in [124], involve studies with a larger number of demonstration discharges, including robustness to hardware failures, and the incorporation of additional physics such as impurity accumulation and NTM dynamics.

## 9. Outlook

Moving forward, TCV will continue to investigate key physics questions in support of ITER and to further develop concepts and operational regimes aimed at optimising the tokamak concept for future fusion power plants, leveraging its strong operational flexibility and versatility. Synergies will be further strengthened across the EUROfusion devices and

with partners beyond, including both public and private initiatives. In the near term, two additional 1 MW dual-frequency gyrotrons will be installed, significantly increasing the available ECRH power. Another upgrade in progress is the installation of a passive in-vessel helical coil, the Runaway Electron Mitigation Coil (REMC), designed to address the challenge of post-disruption runaway-electron beams. During a current quench, the induced currents in the REMC are expected to generate 3D magnetic perturbations that break up nested flux surfaces and suppress RE beam formation [125]. A further major upgrade underway is the testing of the Tightly-Baffled, Long-Legged Divertor (TBLLD) [126], a novel exhaust concept that combines an extended divertor leg with a strong poloidal neutral pressure gradient achieved via tight baffling. This configuration is predicted to enhance power exhaust capabilities by up to a factor of five, while minimising additional engineering complexity, making it attractive for reactor-scale implementation.

Finally, activities around TCV and, more broadly, the SPC will continue to place a high priority on the education and training of the next generation of fusion scientists and engineers. In parallel, research on TCV will also pursue more exploratory topics, such as the properties and performance of the Doublet configuration, which was stabilised successfully for the first time in August 2025 [127]—overcoming a decades-long challenge and opening the door to a new line of investigation.

## Acknowledgment

This work has been carried out within the framework of the EUROfusion Consortium, partially funded by the European Union via the Euratom Research and Training Programme (Grant Agreement No. 101052200 - EUROfusion). The Swiss contribution to this work has been funded in part by the Swiss State Secretariat for Education, Research and Innovation (SERI). Views and opinions expressed are however those of the author(s) only and do not necessarily reflect those of the European Union, the European Commission or SERI. Neither the European Union nor the European Commission nor SERI can be held responsible for them. This work was supported in part by the Swiss National Science Foundation. This work was supported in part by the US Department of Energy under the following Awards: DE-SC0010529, DE-FC02-04ER54698.

## ORCID iDs

C. Theiler 0000-0003-3926-1374
J. Ball 0000-0002-4462-6350
S. Brunner 0000-0001-7588-7476
S. Coda 0000-0002-8010-4971
J. Decker 0000-0003-0220-2653
B.P. Duval 0000-0001-7783-129X
A. Fasoli 0000-0003-4319-5736
I. Furno 0000-0001-8348-1716
O. Février 0000-0002-9290-7413
A.N. Karpushov 0000-0002-5994-0916
M. Kong 0000-0002-2004-3513
B. Labit 0000-0002-0751-8182
A. Merle 0000-0003-1831-5644
A. Pau 0000-0002-7122-3346
M. Podesta 0000-0003-4975-0585
H. Reimerdes 0000-0002-9726-1519
O. Sauter 0000-0002-0099-6675
U.A. Sheikh 0000-0001-6207-2489
D. Testa 0000-0002-6372-882X
L. Villard 0000-0003-3807-9482

## References

[1] Hofmann F. *et al* 1994 Creation and control of variably shaped plasmas in TCV *Plasma Phys. Control. Fusion* **36** B277
[2] Duval B.P. *et al* 2024 Experimental research on the TCV tokamak *Nucl. Fusion* **64** 112023
[3] Joffrin E. *et al* 2024 Overview of the EUROfusion Tokamak Exploitation programme in support of ITER and DEMO *Nucl. Fusion* **64** 112019
[4] Karpushov A.N. *et al* 2023 Upgrade of the neutral beam heating system on the TCV tokamak - second high energy neutral beam *Fusion Eng. Des.* **187** 113384
[5] Siravo U., Dubray J., Elaian H., Fasel D. and Velasco D. 2024 Maintenance and optimization of the TCV power supply *Fusion Eng. Des.* **201** 114277
[6] Molina-Cabrera P. *et al* 2026 Improvements to standard diagnostic preparation and data-quality monitoring in the TCV tokamak *Fusion Eng. Des.* **223** 115578
[7] Labit B. *et al* (the TCV team, the MST1 team and the EUROfusion tokamak exploitation team) 2024 Progress in the development of the ITER baseline scenario in TCV *Plasma Phys. Control. Fusion* **66** 025016
[8] Frassinetti L. *et al* 2026 Peeling limited pedestals in JET, MAST-U and TCV: effect of density and isotope mass in deuterium and tritium-rich plasma on pedestal structure and stability and validation of pedestal predictions for ITER *Nucl. Fusion* **66** 056028
[9] Stagni A. *et al* (the TCV Team and the EUROfusion Tokamak Exploitation Team) 2025 Detachment of type-I ELMy H-mode TCV plasmas via nitrogen seeding and correlations with scrape-off layer properties *67th Annual Meeting of the APS Division of Plasma Physics (DPP)* (*Long Beach, CA, 17–21 November*) (available at: www.aps.org/events/2025/67th-dpp)
[10] Labit B. *et al* 2025 L-H power threshold for neutral beam heated plasmas with deuterium, hydrogen, helium and mixed ion species in TCV *Plasma Phys. Control. Fusion* **67** 055010
[11] Coda S. *et al* 2025 Non-inductive high-performance discharges on TCV on the path to steady state *Preprint: 2025 IAEA Fusion Energy Conf.* (*Chengdu, 13–18 October*) (available at: www.iaea.org/events/fec2025)
[12] Dunne M. *et al* 2025 The physics of elm-free regimes in eurofusion tokamaks *Preprint: 2025 IAEA Fusion Energy Conf.* (*Chengdu, 13–18 October*) (available at: www.iaea.org/events/fec2025)
[13] Labit B. *et al* 2025 Progress in characterising transport in ELM free regimes in TCV *51th European Physical Society Conf. on Plasma Physics* (*Vilnius, Lithuania, 7–11 July*) (available at: https://epsplasma2025.com)
[14] Faitsch M. *et al* 2025 The quasi-continuous exhaust regime in JET *Nucl. Fusion* **65** 024003

[15] Stagni A. *et al* (the TCV Team) 2024 The effect of plasma shaping on high density H-mode SOL profiles and fluctuations in TCV *Nucl. Fusion* **64** 026016
[16] Bernert M. *et al* 2025 X-point radiation: from discovery to potential application in a future reactor *Nucl. Mater. Energy* **43** 101916
[17] Sun G., Pan O., Bernert M., Carpita M., Duval B.P., Février O., Koenders J.T.W., Reimerdes H., Theiler C. and Wiesen S. 2025 SOLPS-ITER simulation of an X-point radiator in TCV (arXiv:2311.07295)
[18] Reimerdes H. *et al* 2024 Access to an ELM-suppressed X-point radiator regime in TCV snowflake minus configurations *Nucl. Mater. Energy* **41** 101784
[19] Fevrier O. *et al* 2026 Core-edge integration of negative triangularity plasmas in TCV *Nucl. Fusion* submitted
[20] Février O. *et al* (the TCV Team and the EUROfusion Tokamak Exploitation Team) 2024 Comparison of detachment in Ohmic plasmas with positive and negative triangularity *Plasma Phys. Control. Fusion* **66** 065005
[21] Tonello E. *et al* (the TCV Team and the WPTE Team) 2024 Modelling of power exhaust in TCV positive and negative triangularity L-mode plasmas *Plasma Phys. Control. Fusion* **66** 065006
[22] Durr-Legoupil-Nicoud G. *et al* 2026 Impact of divertor closure on power exhaust in Negative Triangularity in TCV *Nucl. Fusion* accepted
[23] Lim K., Giacomin M., Ricci P., Coelho A., Février O., Mancini D., Silvagni D. and Stenger L. 2023 Effect of triangularity on plasma turbulence and the SOL-width scaling in L-mode diverted tokamak configurations *Plasma Phys. Control. Fusion* **65** 085006
[24] Morgan R.I. *et al* 2025 Triangularity dependence of the divertor heat flux profile and SOL filamentary turbulence on TCV *Nucl. Fusion* **65** 106030
[25] Mombelli F. *et al* (the TCV team, and the EUROfusion Tokamak Exploitation Team) 2025 Impact of triangularity on edge transport and divertor detachment: a SOLPS-ITER study of TCV L-mode plasmas (arXiv:2506.03966)
[26] Muscente P., Innocente P., Ball J. and Gorno S. 2023 Analysis of edge transport in L-mode negative triangularity TCV discharges *Nucl. Mater. Energy* **34** 101386
[27] Durr-Legoupil-Nicoud G. *et al* 2025 Divertor-core integration in high-performance, negative triangularity plasmas on TCV *51th European Physical Society Conf. on Plasma Physics* (*Vilnius, Lithuania*, *7–11 July*) (available at: https://epsplasma2025.com)
[28] Balestri A., Ball J., Coda S., Cruz-Zabala D.J., Garcia-Munoz M. and Viezzer E. 2024 Physical insights from the aspect ratio dependence of turbulence in negative triangularity plasmas *Plasma Phys. Control. Fusion* **66** 075012
[29] Balestri A. *et al* 2025 Building a path towards a negative triangularity fusion reactor with gyrokinetic simulations and experiments on TCV *51th European Physical Society Conf. on Plasma Physics* (*Vilnius, Lithuania*, *7–11 July*) (available at: https://epsplasma2025.com)
[30] Di Giannatale G., Bottino A., Brunner S., Murugappan M. and Villard L. 2024 System size scaling of triangularity effects on global temperature gradient-driven gyrokinetic simulations *Plasma Phys. Control. Fusion* **66** 095003
[31] Balestri A. *et al* (the TCV Team and the EUROfusion Tokamak Exploitation Team) 2024 Experiments and gyrokinetic simulations of TCV plasmas with negative triangularity in view of DTT operations *Plasma Phys. Control. Fusion* **66** 065031
[32] Mariani A. *et al* (the EUROfusion Tokamak Exploitation team, the TCV Team and the ASDEX Upgrade Team) 2024 Negative triangularity scenarios: from TCV and AUG experiments to DTT predictions *Nucl. Fusion* **64** 106024
[33] Hoppe M. *et al* (the TCV Team and the EUROfusion Tokamak Exploitation Team) 2025 An upper pressure limit for low-Z benign termination of runaway electron beams in TCV *Plasma Phys. Control. Fusion* **67** 045015
[34] Decker J. *et al* (the TCV Team and the EUROfusion Tokamak Exploitation Team) 2024 Expulsion of runaway electrons using ECRH in the TCV tokamak *Nucl. Fusion* **64** 106027
[35] Wijkamp T.A., Hoppe M., Decker J., Duval B.P., Perek A., Sheikh U., Classen I.G.J. and Jaspers R.J.E. (the TCV team) 2023 Resonant interaction between runaway electrons and the toroidal magnetic field ripple in TCV *Nucl. Fusion* **64** 016021
[36] Sheikh U. *et al* 2025 Multi-machine studies of low-Z benign termination of runaway electron beams and extrapolation to ITER *Preprint: 2025 IAEA Fusion Energy Conf.* (*Chengdu*, *13–18 October*) (available at: www.iaea.org/events/fec2025)
[37] Tonello E. *et al* 2025 Modelling companion plasma recombination in runaway benign terminations with SOLPS-ITER *Joint Runaway Electron Modelling (REM) and WPTE RT03 Analysis Meeting,* (*Lausanne*, *2–6 June*) (available at: https://ft.nephy.chalmers.se/?p=conference&id=7)
[38] Simons L., Cerovsky J., Decker J., Duval B.P., Ficker O., Hoppe M. and Sheikh U. (the TCV Team) 2025 A lanthanum bromide detector of runaway electrons for TCV *Rev. Sci. Instrum.* **96** 093501
[39] Poley-Sanjuán J., Simons L., Van Vuuren A.J., Duval B.P., Fasoli A., Karpushov A.N. and Decker J. (the TCV Team) 2025 First velocity-space resolved measurements of relativistic electron losses in a magnetically confined plasma *Nucl. Fusion* **65** 114001
[40] Poley-Sanjuán J. *et al* (the TCV team) 2025 First microsecond velocity-space resolved simultaneous measurements of co- and counter-current fast-ion losses in forward and reverse magnetic field in a tokamak *Nucl. Fusion* **65** 076006
[41] Poley-Sanjuán J. *et al* (the TCV team) 2025 Design and upgrades of the TCV fast ion loss detector *Rev. Sci. Instrum.* **96** 083504
[42] Schmidt B.S. *et al* 2024 A new FILDSIM model for improved velocity-space sensitivity modelling and reconstructions *Plasma Phys. Control. Fusion* **66** 045004
[43] Breizman B.N., Dreval M.B. and Sharapov S.E. (The TCV Team and The EUROfusion Tokamak Exploitation Team) 2025 New interpretation of ion cyclotron emission from a tokamak *Phys. Plasmas* **32** 100702
[44] Ochoukov R. *et al* (TCV Team, ASDEX Upgrade Team and EUROfusion Tokamak Exploitation Team) 2026 Design, installation and first results from the ion cyclotron emission diagnostic on TCV *EPJ Web Conf.* **346** 03009
[45] van Vuuren A.J., Dreval M.B., Ochoukov R., Sharapov S.E., Duval B.P., Elaian H., Simons L., Paraskevopoulos C. and Karpushov A.N. (EUROfusion Tokamak Exploitation and TCV Teams) 2026 First observations of ion cyclotron emission in the TCV tokamak *Nucl. Fusion* submitted
[46] Rud M., Dong Y., Everink J.M., Järleblad H., Jørgensen J.S., Kernel Q., Madsen B., Podestá M., Valentini A. and Salewski M. (the TCV Team) 2026 Bayesian velocity-space tomography with collision- and charge-exchange-physics prior from fast-ion D-alpha measurements at TCV with uncertainty quantification *Plasma Phys. Control. Fusion* **68** 015035
[47] Mazzi S. *et al* 2023 Study of fast-ion-driven toroidal Alfvén eigenmodes impacting on the global confinement in TCV L-mode plasmas *Front. Phys.* **11** 1225787
[48] Dreval M.B. *et al* (the TCV Team and the EUROfusion Tokamak Exploitation Team) 2024 Experimental

investigation of the radial structure of energetic particle driven GAM in TCV *Nucl. Fusion* **65** 016037
[49] Poley-Sanjuán J. *et al* (the EUROfusion Tokamak Exploitation Team and the TCV Team) 2025 First measurements of velocity-space resolved intra-ELM fast-ion losses on the TCV tokamak *Nucl. Fusion* **65** 092006
[50] Van Vuuren A. *et al* 2025 Control of energetic particle modes on the TCV tokamak *Preprint: 2025 IAEA Fusion Energy Conf.* (*Chengdu*, *13–18 October* (available at: www.iaea.org/events/fec2025)
[51] Poley-Sanjuán J. *et al* (EUROfusion Tokamak Exploitation Team and TCV Team) 2026 Dynamics of the fast-ion acceleration in type-I ELMy H-mode scenarios on the TCV tokamak *Nucl. Fusion* **66** 036009
[52] Poley-Sanjuán J., Van Vuuren A.J., Podestá M., Fasoli A., Karpushov A.N. and Duval B.P. (TCV team) 2026 Fast ion confinement in negative triangularity plasmas on the TCV tokamak *Nucl. Fusion* **66** 046012
[53] Tanaka K. *et al* 2025 Isotope effects in linear and saturated ohmic confinement of TCV tokamak and gyrokinetic validation *Nucl. Fusion* **65** 092002
[54] Salmi A. *et al* 2025 Measurements of the intrinsic torque driven by up-down asymmetric L-mode plasmas in TCV *51th European Physical Society Conf. on Plasma Physics* (*Vilnius, Lithuania*, *7–11 July*) (available at: https://epsplasma2025.com)
[55] Marin M. *et al* 2025 Full radius integrated modelling of ohmic ramp-up at TCV including self consistent density prediction *Nucl. Fusion* **65** 036015
[56] Van Mulders S. *et al* (the TCV Team) 2026 Model-based estimation of tokamak plasma profiles and physics parameters: integration with improved equilibrium reconstruction and experimental data *Nucl. Fusion* **66** 026026
[57] Van Mulders S. *et al* 2025 Model-based estimation of tokamak plasma profiles and physics parameters: algorithm overview and application to ITER *Nucl. Fusion* **65** 066006
[58] Hamm D., Theiler C., Simeoni M., Duval B.P., Debarre T., Simons L. and Queralt J.R. 2025 Tomography for plasma imaging: a unifying framework for Bayesian inference *Plasma Phys. Control. Fusion* **67** 115012
[59] Krutkin O., Kumar U., Mazzi S., Brunner S., Coda S., Rienäcker S. and van Rossem M. (the TCV Team) 2024 Validation of short-pulse reflectometry turbulence measurements with a synthetic diagnostic *Nucl. Fusion* **64** 026010
[60] Krutkin O., Brunner S., Coda S. and Combette A. 2025 Nonlinear effects in fluctuation short pulse reflectometry *Plasma Phys. Control. Fusion* **67** 055040
[61] Kumar U., Coda S., Van Rossem M., Porte L., Molina P. and Krutkin O. (the TCV team) 2026 Short pulse reflectometry with direct pulse sampling on the TCV tokamak *Rev. Sci. Instrum.* submitted
[62] Cazabonne J., Coda S., Decker J., Krutkin O., Kumar U. and Peysson Y. (the TCV Team) 2024 Impact of microwave beam scattering by density fluctuations on the electron-cyclotron power deposition profile in tokamaks *Nucl. Fusion* **64** 026019
[63] Cazabonne J. *et al* (the TCV Team) 2023 Experimental and numerical investigations of electron transport enhancement by electron-cyclotron plasma-wave interaction in tokamaks *Plasma Phys. Control. Fusion* **65** 104001
[64] Clod A., Senstius M.G., Nielsen A.H., Ragona R., Thrysøe A.S., Kumar U., Coda S. and Nielsen S.K. 2024 Cascades of parametric instabilities in the tokamak plasma edge during electron cyclotron resonance heating *Phys. Rev. Lett.* **132** 135101
[65] Clod A., Ragona R., Senstius M.G., Jensen T., Kumar U., Coda S. and Nielsen S.K. (the TCV Team) 2024 Utilizing parametric instabilities to diagnose edge density fluctuations in TCV *Plasma Phys. Control. Fusion* **66** 125001
[66] Biwole A.T., Porte L., Coda S. and Fasoli A. (TCV Team) 2023 Vertical electron cyclotron emission diagnostic on the Tokamak à Configuration Variable *Rev. Sci. Instrum.* **94** 103504
[67] Biwole A.T., Porte L., Fasoli A., Figini L., Decker J., Hoppe M., Cazabonne J., Votta L., Simonetto A. and Coda S. (the TCV Team) 2024 Cross-calibration and first vertical ECE measurement of electron energy distribution in the TCV tokamak *Plasma Phys. Control. Fusion* **66** 125010
[68] Rienäcker S., Hennequin P., Vermare L., Honoré C., Coda S., Labit B., Vincent B., Wang Y., Frassinetti L. and Panico O. (the TCV team and the EUROfusion Tokamak Exploitation team) 2025 Survey of the edge radial electric field in L-mode TCV plasmas using Doppler backscattering *Plasma Phys. Control. Fusion* **67** 065003
[69] Rienäcker S. *et al* (the TCV Team) 2025 Edge radial electric field in positive and negative triangularity plasmas in the TCV tokamak *Nucl. Fusion* **66** 014002
[70] Krutkin O., Chapman-Oplopoiou B., Frassinetti L., Brunner S., Coda S. and Labit B. (the TCV team and the EUROfusion Tokamak Exploitation Team) 2025 Modelling of ETG turbulent transport in the TCV pedestal *Plasma Phys. Control. Fusion* **67** 025029
[71] Ugoletti M. *et al* (TCV Team and WPTE Team) 2024 Role of radiation re-absorption in the thermal helium beam diagnostic *Rev. Sci. Instrum.* **95** 083530
[72] Matina M.L. *et al* 2025 Experimental characterization of inter-ELM modes in type-I ELMy scenarios at TCV using the thermal helium beam diagnostic *Plasma Phys. Control. Fusion* **67** 085034
[73] Griener M., Wüthrich C., Wang Y., Brida D., Faitsch M., Offeddu N. and Theiler C. (the TCV Team and the EUROfusion Tokamak Exploitation Team) 2024 Characterization of the I-phase regime at TCV *Nucl. Fusion* **65** 016041
[74] Ducker R., Mykytchuk D., Duval B.P., Reimerdes H., Andrebe Y., Landis J.D., Lee K. and Perek A. (TCV Team) 2025 High-resolution visible spectroscopy for ion temperature and flow velocity measurements of the TCV divertor plasma *Rev. Sci. Instrum.* **96** 123503
[75] Martinelli L. *et al* (the TCV team) 2025 Interpretation of divertor ion temperature measurements from an attached towards a detached regime *Nucl. Fusion* **65** 056017
[76] Sun G., Reimerdes H., Elaian H., Baquero-Ruiz M., Brown B., Gospodarczyk M., Noël M. and Tonello E. 2025 Neutral pressure measurement in TCV tokamak using ASDEX-type pressure gauges *Rev. Sci. Instrum.* **96** 083502
[77] Cavedon M. *et al* (the ASDEX Upgrade Team, the TCV Team and the EUROfusion Tokamak Exploitation Team) 2025 Separatrix ion to electron temperature ratio in the TCV and ASDEX Upgrade tokamaks *Nucl. Fusion* **65** 106007
[78] Cornelissen M.J.H. *et al* 2026 Coherence imaging spectroscopy with a polarization-sensitive sensor to visualize the plasma flows in fusion devices *Plasma Phys. Control. Fusion* **68** 025022
[79] Verhaegh K. *et al* (the TCV Team and the EUROfusion MST1 Team) 2023 Investigating the impact of the molecular charge-exchange rate on detached SOLPS-ITER simulations *Nucl. Fusion* **63** 076015

[80] Osborne N. *et al* (the Eurofusion Tokamak Exploitation Team, the MAST-U Team and the TCV Team) 2025 A novel understanding of the role of plasma-molecular kinetics on divertor power exhaust *Nucl. Fusion* **65** 116010
[81] Sun G. *et al* (the EUROfusion Tokamak Exploitation Team and the TCV Team) 2025 Investigating the influence of divertor baffles on nitrogen-seeded detachment in TCV with SOLPS-ITER simulations and TCV experiments *Nucl. Fusion* **65** 026061
[82] Yang H. *et al* 2023 Numerical study of divertor detachment in TCV H-mode scenarios *Plasma Phys. Control. Fusion* **65** 125005
[83] Wang Y., Colandrea C., Oliveira D.S., Theiler C., Reimerdes H., Body T., Galassi D., Martinelli L. and Lee K. (the TCV Team) 2024 Validation of SOLPS-ITER simulations against the TCV-X21 reference case *Nucl. Fusion* **64** 056040
[84] Tonello E. *et al* 2025 Advancing SOLPS-ITER validation with TCV L-mode discharges *Nucl. Fusion* **66** 066015
[85] Février O., Gorno S., Theiler C., Carpita M., Durr-Legoupil-Nicoud G. and von Allmen M. 2024 SPLEND1D, a reduced one-dimensional model to investigate the physics of plasma detachment *Phys. Plasmas* **31** 082502
[86] Derks G.L., Westerhof E., van Berkel M., Jenneskens J.H., Koenders J.T.W., Mijin S., Moulton D., Reimerdes H. and Wu H. 2024 Multi-machine benchmark of the self-consistent 1D scrape-off layer model DIV1D from stagnation point to target with SOLPS-ITER *Plasma Phys. Control. Fusion* **66** 055004
[87] Molina-Cabrera P.A., Felici F., Coda S., Merle A., Simons L., Heiss C., Galperti C., Perek A. and Wüthrich C. (the TCV Team) 2025 Electromagnetic analysis of breakdown conditions and experimental validation of 0D Townsend breakdown theory on the TCV tokamak *Nucl. Fusion* **65** 106005
[88] Verhaegh K. *et al* 2025 The physics basis for implementing alternative divertor configurations on reactors *Preprint: 2025 IAEA Fusion Energy Conf.* (*Chengdu*, *13–18 October*) (available at: www.iaea.org/events/fec2025)
[89] Carpita M., Tonello E., Colandrea C., Février O., Reimerdes H., Sun G. and Mombelli F. 2025 Verification of techniques for accelerated and stable SOLPS-ITER simulations including plasma drifts *Nucl. Fusion* **65** 116001
[90] Carpita M. *et al* 2025 Assessment of alternative divertor configurations in TCV via experiments and interpretative SOLPS-ITER modelling *9th Asia-Pacific Conf. on Plasma Physics* (*Fukuoka*, *21–26 September*) (available at: www.aappsdpp.org/DPP2025/)
[91] Lee K. *et al* 2025 *X*-Point Target Radiator Regime in Tokamak Divertor Plasmas *Phys. Rev. Lett.* **134** 185102
[92] Winkel M.W.G. *et al* (TCV Team and EUROfusion Tokamak Exploitation Team) 2026 private communication
[93] Lee K. *et al* 2025 The prospects of an X-point target radiator as a reactor exhaust solution *67th Annual Meeting of the APS Division of Plasma Physics (DPP)* (*Long Beach, CA*, *17–21 November*) (available at: www.aps.org/events/2025/67th-dpp)
[94] Zurita M. *et al* 2025 Mitigation of edge-localized modes with an X-point target divertor in TCV *67th Annual Meeting of the APS Division of Plasma Physics (DPP)* (*Long Beach, CA*, *17–21 November*) (available at: www.aps.org/events/2025/67th-dpp)
[95] Lim K., Ricci P., Stenger L., De Lucca B., Durr-Legoupil-Nicoud G., Février O., Theiler C. and Verhaegh K. 2024 Predictive power-sharing scaling law in double-null L-mode plasmas *Nucl. Fusion* **64** 106057
[96] Moiraf D. *et al* 2026 Impact of triangularity on power sharing and boundary turbulence in TCV double-null L-mode plasmas *Nucl. Fusion* submitted
[97] Mancini D., Ricci P., Vianello N., Van Parys G. and Oliveira D.S. 2023 Self-consistent multi-component simulation of plasma turbulence and neutrals in detached conditions *Nucl. Fusion* **64** 016012
[98] Wang Y., Wüthrich C., Theiler C., García Herreros S., Oliveira D.S., Mancini D., Golfinopoulos T., Ricci P. and Body T. and (TCV Team) 2026 Comparison of filament properties in real-size GBS simulations and experiments of TCV-X21 *Plasma Phys. Control. Fusion* (https://doi.org/10.1088/1361-6587/ae6d71)
[99] Tsui C.K., Boedo J.A., Myra J.R., Galassi D. and Wüthrich C. (TCV Team) 2024 Divertor turbulent transport in the single null and snowflake in the TCV tokamak *Phys. Plasmas* **31** 022506
[100] Rizkallah R., Boedo J.A., Tsui C.K. and Perillo R. 2026 Enhanced turbulent transport and drift reduction in divertors at the detachment onset *Nucl. Fusion* **66** 046028
[101] Mele A., Tenaglia A., Felici F., Galperti C., Carnevale D., Coda S., Merle A., Pironti A. and Sauter O. (the TCV team and the Eurofusion Tokamak Exploitation team) 2025 Design and implementation of a model-based hierarchical architecture for plasma shape control in the TCV tokamak *Plasma Phys. Control. Fusion* **67** 065035
[102] Galperti C. *et al* 2024 Overview of the TCV digital real-time plasma control system and its applications *Fusion Eng. Des.* **208** 114640
[103] Masocco R., Tenaglia A., Galperti C., Carnevale D. and Galeani S. 2025 A distributed real-time diagnostic and control network for the TCV tokamak based on the Data Distribution Service *Fusion Eng. Des.* **221** 115344
[104] di Grazia L.E. *et al* (the TCV Team) 2024 Automated shot-to-shot optimization of the plasma start-up scenario in the TCV tokamak *Nucl. Fusion* **64** 096032
[105] Marchioni S. 2024 Vertical instability studies in the TCV tokamak and development and application of multimachine real-time proximity control strategies *PhD Thesis* École Polytechnique Fédérale de Lausanne (EPFL)
[106] Dubbioso S., De Tommasi G., Galperti C., Felici F., Marchioni S., Mele A., Merle A. and Tenaglia A. 2025 Simulation validation of an Extremum Seeking-based Vertical Stabilization system for TCV *Fusion Eng. Des.* **219** 115198
[107] Tenaglia A., Pesamosca F., Felici F., Carnevale D., Coda S., Mele A. and Merle A. 2024 An interpretable isoflux-based observer for plasma shape control errors in tokamaks *Fusion Eng. Des.* **207** 114618
[108] Mele A., Topalova M.A., Galperti C. and Coda S. 2025 First experimental demonstration of plasma shape control in a tokamak through model predictive control *2025 IEEE Conf. on Control Technology and Applications (CCTA)* (*San Diego, CA, USA*, *25–27 August*) pp 820–5
[109] Tracey B.D. *et al* 2024 Towards practical reinforcement learning for tokamak magnetic control *Fusion Eng. Des.* **200** 114161
[110] Frattolillo D. *et al* (TCV Team and Eurofusion Tokamak Exploitation Team) 2025 Implementation of an ITER-relevant QP-based current limit avoidance algorithm in the TCV tokamak *Plasma Phys. Control. Fusion* **67** 055017
[111] Tenaglia A., Masocco R., Mele A., Carnevale D., Coda S., Felici F., Galeani S., Merle A. and Sassano M. 2024 Dynamic steady-state coil current allocation for plasma shape control: a study on the TCV tokamak *2024 10th Int. Conf. on Control, Decision and Information Technologies (CoDIT)* (*Vallette, Malta, 1–4 July*) pp 278–83

[112] Pastore F., Felici F., Bosman T.O.S.J., Galperti C., Sauter O., Vincent B. and Vu N.M.T. 2023 Model-based electron density estimation using multiple diagnostics on TCV *Fusion Eng. Des.* **192** 113615
[113] Pastore F. *et al* (the TCV team, and the EUROfusion Tokamak Exploitation Team) 2025 Applications of a novel model-based real-time observer for electron density profile control experiments in TCV
[114] Contré C.E. *et al* (the TCV team and the EUROfusion Tokamak Exploitation Team) 2026 Kinetic Equilibrium Prediction at TCV using RAPTOR and FBT *Nucl. Fusion* submitted
[115] Poels Y., Venturini C., Pau A., Sauter O. and Menkovski V. (the TCV Team and the WPTE Team) 2025 Robust confinement state classification with uncertainty quantification through ensembled data-driven methods *Nucl. Fusion* **65** 096022
[116] Poels Y., Pau A., Donner C., Romanelli G., Sauter O., Venturini C. and Menkovski V. (the TCV Team and the WPTE Team) 2025 Plasma state monitoring and disruption characterization using multimodal VAEs *Nucl. Fusion* **65** 096012
[117] Sieglin B. *et al* 2025 H-Mode density limit disruption avoidance in ASDEX Upgrade, TCV and JET *Fusion Eng. Des.* **215** 114961
[118] Ravensbergen T. *et al* 2025 A Simulink-based platform for model-based design and deployment of controllers for tokamak nuclear fusion devices *IFAC-PapersOnLine* **59** 192–7
[119] Pesamosca F. *et al* 2025 Real-time implementation of ITER first wall heat load control modules on TCV *31st IEEE Symp. on Fusion Engineering (SOFE 2025)* (*Cambridge, MA, USA*, *23–26 June*) (available at: www.psfc.mit.edu/sofe2025/)
[120] Bosman T.O.S.J. 2025 Density profile and heat-exhaust control in nuclear fusion devices: development of control methods in view of the operation of fusion power plants *PhD Thesis* Eindhoven University of Technology
[121] van Berkel M. *et al* (the EUROfusion Tokamak Exploitation Team, the AUG Team, the DIII-D Team, the JET Team, the MAST-U Team, the TCV Team and the WEST Team) 2026 Systematic multi-machine analysis of the exhaust time-dependent behavior in tokamaks *Nucl. Fusion* **66** 036017
[122] Derks G.L. 2026 Dynamic exhaust modeling for fusion reactors *PhD Thesis* Eindhoven University of Technology
[123] van Leeuwen L., Schoukens M., Citrin J., van Berkel M., Duval B. and Perek A. (the TCV Team) 2025 Machine learning enhanced tomographic reconstruction for multispectral imaging on TCV *Plasma Phys. Control. Fusion* **67** 025024
[124] Wang A.M. *et al* 2025 Learning plasma dynamics and robust rampdown trajectories with predict first experiments at TCV *Nat. Commun.* **16** 8877
[125] Battey A. *et al* 2026 private communication
[126] Reimerdes H. *et al* 2026 Implementation of a tightly baffled long-legged divertor in TCV *Nucl. Fusion* (https://doi.org/10.1088/1741-4326/ae69f9)
[127] Heiss C. *et al* 2025 First achievement of stationary doublet plasmas in the TCV Tokamak *Invited Talk at the 67th Annual Meeting of the APS Division of Plasma Physics (DPP)* (*Long Beach, CA*, *17–21 November*) (available at: www.aps.org/events/2025/67th-dpp)